

UNIVERSIDAD DE LA LAGUNA

TRABAJO DE FINAL DE MASTER

MASTER THESIS

---

# Unveiling the Ionisation Continuum in Low-Luminosity AGN

---

*Author*

Xavier LÓPEZ LÓPEZ

*Supervisor*

Almudena PRIETO ESCUDERO

6 de julio de 2020



## Agradecimientos

*A mi madre, a mis dos padres, y a mi hermano, por quererme, apoyarme siempre, y por seguir escuchando cuando les intento explicar qué es un LLAGN.*

*A mi tutora, Almudena, por motivarme desde el primer día a realizar esta investigación y sumergirme en el apasionante y complejísimo mundo de los AGN. Por impulsarme siempre a hacerme las preguntas necesarias y no dar nada por sentado.*

*Y por supuesto, a Juan Antonio Fernández Ontiveros. Por hacerme entender el hilo conductor de este trabajo. Por enseñarme tanta física y astrofísica. Por las innumerables horas enseñándome a escribir un trabajo científico. Porque me ha impresionado como científico y como persona. Y por todo el material que me ha pasado, en forma de código, imágenes o bibliografía, que me ha permitido realizar este trabajo.*

# Contents

<b>Abstract</b>	<b>3</b>
<b>Resumen</b>	<b>4</b>
<b>1. Introduction</b>	<b>6</b>
1.1. Active Galactic Nuclei . . . . .	6
1.1.1. Observational Properties . . . . .	7
1.1.2. Unification Models . . . . .	8
1.2. Accretion . . . . .	10
1.2.1. Eddington Limit . . . . .	10
1.2.2. Accretion Discs . . . . .	11
1.3. Low Luminosity AGN . . . . .	13
1.3.1. Accretion Flow at Low Accretion Rates . . . . .	14
1.3.2. The Ionising Continuum in LLAGN . . . . .	15
1.4. Aim of this work . . . . .	15
<b>2. Dataset and Methodology</b>	<b>16</b>
2.1. The Sample . . . . .	16
2.2. High Angular Resolution SEDs . . . . .	16
2.3. Emission-line spectrum . . . . .	17
2.4. Methodology . . . . .	19
2.4.1. Fitting the SEDs . . . . .	19
2.4.2. Photoionisation Simulations . . . . .	19
<b>3. Results</b>	<b>21</b>
3.1. The continuum shape at high-angular resolution . . . . .	21
3.2. Power law + Accretion disc models . . . . .	22
3.3. Dependence with the spectral index . . . . .	27
3.4. Jet Model Comparison . . . . .	28

---

3.5. Contribution of the accretion disc to the ionisation . . . . .	32
<b>4. Discussion</b>	<b>33</b>
4.1. The Ionisation Continuum in LLAGN . . . . .	33
4.2. Ionisation by a Jet Continuum . . . . .	34
4.3. The Accretion Disc Contribution . . . . .	34
4.4. Outliers . . . . .	35
<b>5. Conclusions</b>	<b>36</b>

**Abstract**

The accretion disc of low-luminosity active galactic nuclei (LLAGN) is predicted to disappear at low Eddington ratios ( $L_{\text{bol}}/L_{\text{edd}} < -3$ ), while high-angular resolution observations of these nuclei have revealed a steep power law optical/UV continuum with  $\alpha \sim 2$  ( $F_{\nu} \sim \nu^{-\alpha}$ ), characteristic of synchrotron emission. However, hydrogen absorption makes it impossible to probe this continuum shortwards of  $\sim 1000 \text{ \AA}$ , and thus the possible contribution of an accretion disc cannot be fully discarded. Still, this information is encoded in the fine structure lines produced by the AGN ionised gas, whose relative intensities are sensitive to the shape of the ionising continuum and therefore can be used to probe the presence of the accretion disc. In this work we have combined diffraction-limited high-angular resolution observations from the *Hubble Space Telescope* in the optical/UV range and the Very Large Telescope in the near- to mid-infrared (IR) range for a sample of 10 LLAGN. These direct measurements of the accessible part of the LLAGN continuum have been combined with photo-ionisation simulations using CLOUDY and mid-IR fine-structure lines observed by *Spitzer*, to infer the shape of the missing continuum below  $\sim 1000 \text{ \AA}$ . This approach allowed us to reconstruct the primary ionising spectra and the disc contribution in prototypical LLAGN nuclei such as M87, NGC 1052, or the Sombrero galaxy. The IR emission line properties of the LLAGN in our sample can be reproduced by a power law continuum extending from the UV to the X-ray range, with a typical index of  $0.35 \lesssim \alpha \lesssim 0.55$ , with a negligible or no contribution at all from the accretion disc to the ionisation. These accretion discs must be truncated or in a cool state in order to explain the lack of ionising photons. The power law component dominating the extreme UV continuum in LLAGN is associated with inverse Compton emission from reprocessed synchrotron jet emission by the black hole corona. This is supported by photo-ionisation predictions for jet models applied to three of the LLAGN in our sample.

## Resumen

Diversas líneas de investigación, tanto teóricas como observacionales, apuntan a la existencia de un agujero negro supermasivo (SMBH, por sus siglas en inglés<sup>1</sup>: *Super Massive Black Hole*) en el centro de todas las galaxias masivas ( $M_* \gtrsim 10^{10} M_\odot$ ). Además, en muchos casos se observan altas luminosidades y/o grados de ionización en estos núcleos que no pueden explicarse por actividad estelar; estas regiones se conocen como núcleos activos de galaxias (AGN, por *Active Galactic Nuclei*). La masa del SMBH parece estar directamente correlacionada con diversas propiedades del bulbo de su galaxia huésped, lo cual sugiere la existencia de un periodo de evolución común entre la propia galaxia y su agujero negro central. Procesos relacionados con el SMBH y que conllevan la expulsión de grandes cantidades de masa y/o energía al medio galáctico podrían llegar a regular la formación estelar en estas galaxias durante ciertos periodos de especial actividad. Por lo tanto, el estudio de los AGN es una herramienta clave a la hora de entender la formación y evolución de las galaxias actuales.

Hoy en día existe un consenso ampliamente extendido en la comunidad científica acerca del origen de las altas luminosidades observadas en estos núcleos, que se resume en el modelo unificado de los AGN. Según este modelo, en el centro de cada AGN hay un agujero negro supermasivo, con una masa en el rango  $M_{\text{BH}} \sim 10^6 - 10^9 M_\odot$ . Alrededor de este se produce un flujo constante de materia cayendo hacia el SMBH, que se da en forma de un disco de acreción geoméricamente delgado y ópticamente grueso, con una alta eficiencia de conversión materia-energía. Este llega a su máximo de emisión en el rango UV, por lo que se asume que es el responsable de la fotoionización en estos núcleos. Más allá del disco existiría un toro de gas y polvo frío, que alimenta al disco de material, y también explicaría cierto grado de variedad observacional que presentan los núcleos activos de galaxias.

En este trabajo nos centraremos en AGN de baja luminosidad (LLAGN, por *Low-Luminosity AGN*;  $L_{\text{bol}}/L_{\text{edd}} < -3$ ). Estos núcleos representan la clase más abundante de AGN, siendo observados en aproximadamente una de cada tres galaxias del Universo local. Los modelos teóricos para estos AGN de baja luminosidad predicen cambios estructurales que se alejarían del modelo unificado, como la desaparición del toro, o la sustitución del disco de acreción geoméricamente delgado y ópticamente grueso de alta eficiencia por una estructura mucho menos eficiente radiativamente. Una posible alternativa sería un disco de acreción truncado a un cierto radio. Este, al ser mucho más frío que un disco clásico, emitiría la mayor parte de su radiación electromagnética a bajas energías (IR o visible), lo que plantea la siguiente cuestión: ¿Cuál es el mecanismo responsable de la fotoionización en los LLAGN? Y por otra parte, ¿qué forma tiene el continuo ionizante procedente de estos núcleos?

El presente trabajo intenta arrojar algo de luz sobre la solución a estas preguntas. Para ello, usamos datos de muy alta resolución espacial obtenidos para una muestra compuesta por 10 LLAGN. Debido a la baja luminosidad de estos núcleos, la alta resolución de los datos es un elemento clave, ya que los datos de baja resolución usados comúnmente en la literatura incluyen contaminación estelar, que en muchos casos domina sobre la emisión nuclear. De la muestra estudiada, nos fijamos en concreto en la distribución espectral de flujo de 4 de estos objetos, elegidos como representativos de toda la muestra (y posiblemente de toda la clase LLAGN), y ajustamos esta a un modelo de ley de potencias ( $F_\nu \sim \nu^\alpha$ ) más un disco de acreción truncado. Los datos de los que disponemos cubren prácticamente todo el espectro electromagnético desde bajas a altas energías, lo cual nos permite que el ajuste cubra todo este rango. La ley de potencias se separa en tres rangos, cada uno caracterizado por un índice espectral  $\alpha$  diferente: desde radio al infrarrojo, del IR al ultravioleta, y del UV a los rayos-X. Algunos objetos, además, han sido ajustados usando un modelo de *jet*. A continuación, los ajustes así creados son utilizados como parámetro de entrada en el código CLOUDY para generar modelos de fotoionización asociados al continuo ionizante de cada LLAGN. El resultado de estos modelos puede ser comparado con observaciones de alta resolución de líneas de emisión del IR medio correspondientes a transiciones de estructura fina y medidas con el espectrógrafo IRS a bordo de Spitzer. En concreto, esta comparación se realiza a través

<sup>1</sup>A lo largo de este resumen se usan varias siglas que provienen del inglés, como SMBH o AGN.

de los llamados diagramas de diagnóstico, en los que cada eje muestra el cociente de dos líneas dadas. El procedimiento aquí descrito se realiza también para el AGN 3C 273, un quasar clásico con un disco de acreción prominente.

Los principales resultados obtenidos con este procedimiento son: *i)* los cocientes de líneas observados son reproducidos satisfactoriamente usando los modelos con leyes de potencias y discos de acreción truncados. La contribución del disco a la ionización es despreciable en todos los casos. *ii)* En general, y salvo algunas excepciones, cada modelo, construido a partir del continuo de un solo LLAGN, es capaz de reproducir los cocientes de líneas observado en otros núcleos. Esto es indicativo de que todos estas fuentes están caracterizadas por continuos ionizantes similares. En concreto, los índices espectrales ajustados están en el rango  $-0,08 < \alpha < 0,26$  para radio,  $1,20 < \alpha < 2,58$  en el rango IR/UV, y  $\alpha \sim 0,45$  (excepto por M87, con  $\alpha = 1,2$ ) en rayos X; es decir, la distribución espectral de flujo es relativamente plana en radio y rayos X, con una caída abrupta en el visible/UV. *iii)* Los modelos basados en un jet compacto también reproducen en general los cocientes de líneas observados. Esto es coherente con la forma del continuo descrita en el punto anterior, donde la emisión de radio hasta UV estaría dominada por radiación sincrotrón, y los rayos X por efecto Compton inverso.

# 1. Introduction

There are strong observational evidences supporting the presence of supermassive black holes (SMBH;  $M_{\text{BH}} \sim 10^6\text{--}10^9 M_{\odot}$ ) in the nucleus of essentially every massive galaxy ( $M_{\star} \gtrsim 10^{10} M_{\odot}$ ; Magorrian et al. 1998; Kormendy & Ho 2013). Besides, the mass of this BH is tightly related to several properties of its host galaxy bulge (like velocity dispersion of the stars, stellar mass and luminosity; Ferrarese & Merritt 2000). This suggests that massive BHs and their host galaxies have grown together during a common evolutionary phase, a scenario supported by observations of star formation at high-redshift galaxies (Madau & Dickinson 2014) and the larger fraction of active nuclei among quenched (passive) galaxies (Heckman & Best 2014). Galaxies with very massive but (currently) passive BHs at their nucleus might have gone through active AGN phases in the past. During this phase, their BHs grow through gas accretion (Rees 1984; Marconi et al. 2004), while releasing large amounts of energy to the ISM via outflows and radiation, a process known as AGN feedback and that has a great impact on regulating star formation (Harrison 2017; Martín-Navarro et al. 2018). Therefore, the study of AGN phenomena, and specifically low-luminosity AGN (LLAGN), is directly connected to the formation and evolution of present-day galaxies.

This active AGN phase represents only a short fraction of the total life of the galaxy; AGN spend most of their lives in a low-luminosity state. In fact, about  $\sim 1/3$  of all the galaxies in the nearby Universe host a low-luminosity AGN in their nuclei (Ho 2008). The accretion mechanism and the role of the accretion disc at these objects is still not well understood. This is caused by observational limitations due to: *i*) heavy absorption of extreme-UV emission, where the peak of the accretion disc is expected, due to hydrogen in the host galaxies of massive BHs and in our own Galaxy; *ii*) contamination by stellar light of these faint nuclei, which typically dominate the integrated light in LLAGN when seeing-limited apertures are used. In fact, it is not even clear that an accretion disc exists at LLAGN, which raises questions on the origin of its power supply and the mechanisms leading to the observed spectrum. The present work tries to shed some light on these questions.

Section 1.1 briefly describes the main aspects of the AGN phenomena, focusing particularly on low-luminosity AGN. In Section 1.2 we introduce the basic theory of accretion and thin accretion discs. Finally, in Section 1.3 we explain the modifications to accretion theory and observations describing LLAGN.

## 1.1. Active Galactic Nuclei

The central region of some galaxies emits large amounts of radiation across basically the whole electromagnetic spectrum, from radio to gamma-rays, sometimes with high luminosities of up to  $L_{\text{bol}} \approx 10^{47} \text{ erg s}^{-1}$ ; these regions are called Active Galactic Nuclei (AGN), and the galaxies that host them are therefore called active galaxies. The observed radiation comes from a compact, spatially unresolved region where matter is being accreted onto a supermassive black hole. Release of gravitational potential energy into heat and radiation, with a much higher mass-to-light conversion efficiency than nuclear fusion<sup>2</sup>, could explain the observed luminosities with accretion rates of only a few solar masses per year (see equation 3).

This accretion flow is commonly assumed to take place through a thin accretion disc (Section 1.2.2). Because of its angular momentum, the infalling gas naturally tends to accumulate in a plane. Viscosity is the key element of this disc: it allows the gas to transfer outwards its net angular momentum so that it can spiral into the central BH (and eventually be advected). In this process, a considerable fraction of the gas

<sup>2</sup>An efficiency of  $\sim 10\%$  is commonly assumed for AGN, whereas the most favourable case of nuclear fusion, which is hydrogen burning, has an efficiency of 0.7% in the conversion of rest mass to energy.



gravitational energy is converted into radiation (especially in the optical and UV range), while the rest is converted into kinetic energy or heat.

Apart from thermal radiation associated with a disc, many AGN also exhibit non-thermal emission. Radio and high-energy fluxes are dominated respectively by synchrotron emission and inverse Compton, which are associated to relativistic outflows of collimated plasma (jets) ejected along the axis of the system and to the energy distribution of particles in the BH corona.

In the next sections, we will see how AGN are classified into a large variety of sub-classes, and also how all this diversity is tried to be understood as variations of a few physical parameters from a unified scheme.

### 1.1.1. Observational Properties

AGN present a rich phenomenology that has motivated historical classifications including a large variety of types and sub-types associated with a complex diversity of observational characteristics (e.g. [Heckman & Best 2014](#)). These classifications have been made attending to different criteria, such as the width of the emission lines in the optical spectra, the relative strength of the radio band with regard to the optical, or the total bolometric luminosity. A short overview of this classification is presented here to introduce the subject of this work; for a much deeper view on the various classifications, we refer to [Padovani et al. \(2017\)](#).

In his pioneering work, [Seyfert \(1943\)](#) discovered that bright nuclei found in a number of nearby galaxies exhibited particularly strong emission lines in their optical spectra, corresponding to highly-excited transitions. Galaxies with these attributes are now called Seyfert galaxies. Their spectra, in the most general case, is formed by both broad and narrow emission lines. The broad lines correspond to allowed atomic transitions (e.g.  $H\alpha$ ) and the narrow ones arise from both allowed and forbidden transitions (e.g.  $[OII]\lambda 3727$ ). Nuclei where these two types of lines are detected are classified as Seyfert I, while those exhibiting only narrow lines are called Seyfert II<sup>3</sup> ([Khachikian & Weedman 1971](#)). These two families of lines arise from different regions: the *broad line region* (BLR), a high-density region close to the nucleus, formed by fast-moving gas clouds accelerated by the BH with typical Doppler broadenings of  $\Delta v_{FWHM} \sim 1-5 \times 10^3 \text{ km s}^{-1}$ ; and the *narrow line region* (NLR), that in comparison to the BLR is less dense, farther away from the nucleus, and moving at lower speeds ( $\Delta v_{FWHM} \sim 5 \times 10^2 \text{ km s}^{-1}$ ). The low densities of the NLR allow forbidden transitions to take place: at higher densities (BLR), these transitions are suppressed by collision before the atom has time to de-excite radiatively.

A crucial step in the understanding of AGN came twenty years later ([Schmidt 1963](#)), with the discovery of *quasars*. Radio sources were identified with point-like optical objects, showing strong broad emission lines at high redshift. However, because of the observed differences between these *quasi-stellar radio sources* and Seyfert galaxies, it still took some years until these were interpreted as two different manifestations of the same phenomena. The radio-quiet counterparts of quasars have also been identified, and they are known as *quasi-stellar objects* (QSOs), although the term quasar is used indistinctly in the literature. Most quasars are type 1 AGN. Radio-loud galaxies of intermediate luminosity are distinguished between *broad-line radio galaxies* (BRGs) and *narrow-line radio galaxies* (NRGs) for type 1 and 2 respectively. Today, radio-loudness is associated with synchrotron radiation coming from relativistic jets or a compact radio-core.

While quasars represent the brightest type of AGN, most AGN are found in a much less luminous state, often even outshined by its host galaxy. Strong emission lines corresponding to atomic and ionic species with low ionisation potentials are commonly detected in these faint nuclei, which are known as *low ionisation nuclear emission regions*, or LINERs ([Heckman 1980](#)). Typical strong lines in the spectrum of LINERs are,

<sup>3</sup>This separation between type 1 and 2 is extended to other types of AGN.

e.g.  $[\text{N II}]\lambda 6584$ ,  $[\text{O I}]\lambda 6300$  and  $[\text{S II}]\lambda 6717, 6731$ ). While these lines are also detected in other types of AGN, their relative strength indicates a lower mean ionisation state in LINERs. Emission line diagnostics diagrams, which compare the relative intensity of two pairs of lines, are a common and efficient tool to separate LINERs from other objects like star-forming galaxies. One example of such a diagram is shown in Figure 1. Just as other types of AGN, LINERs are also classified into type 1 and type 2 sources.

One remark should be done here regarding nomenclature: it is important to note that the defining property of LINERs is the relative strength of emission lines from lowly-ionised species. However, because they are commonly hosted in low-luminosity nuclei, LINERs are often called low-luminosity active galactic nuclei (LLAGN) in the literature. We would like to emphasise the fact that LLAGN and LINER refer to different categories, although it is very common that a source will be a LINER and a LLAGN at the same time. Yet, it is not always the case that a LINER is a LLAGN or vice versa. LLAGN shall be treated in much more detail in Section 1.3.

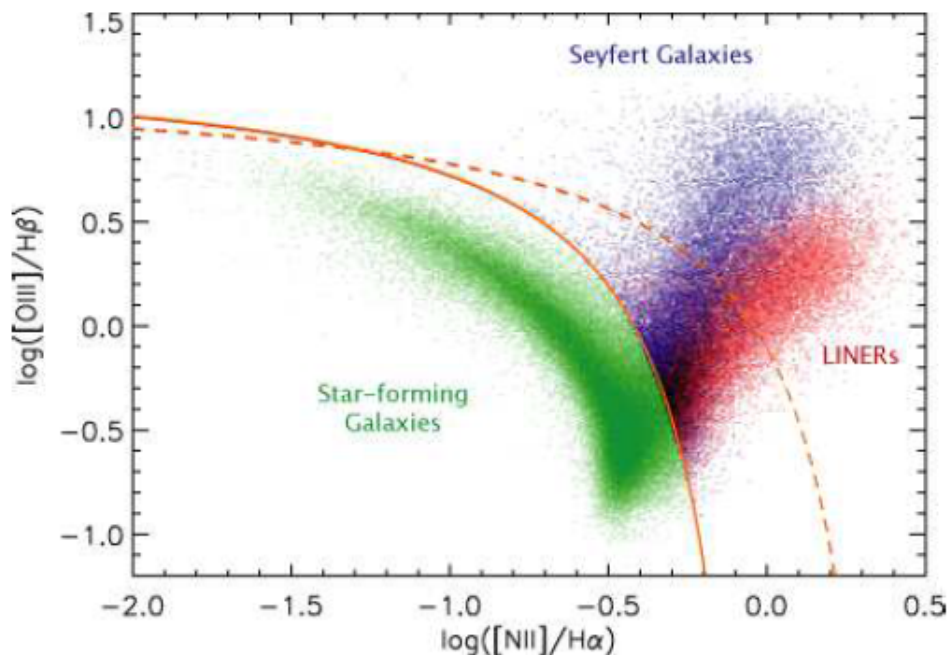


**Figure 1:** Emission line ratio diagnostics diagram of  $[\text{N II}]\lambda 6584/\text{H}\alpha$  versus  $[\text{O III}]\lambda 5007/\text{H}\beta$  for SDSS emission-line galaxies. BPT diagrams (Baldwin et al. 1981) like this one are used to separate star-forming galaxies, Seyferts and LINERs. The solid and dashed curves indicate respectively the empirical and theoretical dividing lines between AGN and star-forming galaxies. Sources that lie in the separation line are considered to have both an AGN and a star-formation component. Reproduced from Groves et al. (2006).

### 1.1.2. Unification Models

The aim of unification models is to explain the wide variety of observational properties described in Section 1.1.1 as a function of a relatively small number of parameters, taking also into account the possible observational biases associated with the selection techniques (Padovani et al. 2017).

The unified models reviewed in Antonucci (1993) and Urry & Padovani (1995) share a common view of the AGN inner structure, where all AGN have the following components: *i*) a supermassive black hole

(SMBH) at its centre, with a typical mass of  $10^6$ – $10^9 M_\odot$ ; *ii*) a strong accretion flow, typically assumed to be through a slim disc (Section 1.2.2); *iii*) a torus of cold gas and dust surrounding the accretion disc, as well as smaller gas clouds moving at different speeds, which form the broad line region (BLR) and narrow line region (NLR). This torus is a key component of unification models, as it is used to explain the observed dichotomy between type 1 and 2 AGN; when AGN are observed nearly edge-on, the torus shields the nucleus and the BLR and we observe a type 2 AGN. On the other hand, on type 1 AGN the orientation of the torus allows us to directly detect the BLR. Besides, the torus fulfils two other important roles: it acts as a source of gas and molecular material that feed the accretion flow, and it collimates radiation from the NLR, which is observed with the shape of a cone in many galaxies. The opening angle of this cone is determined by the shape of the torus.

Another important feature of unification models, which is however not included in all of them, are jets. These are collimated outflows of charged particles, which are accelerated at relativistic speeds along the axis of the disc, and whose size range from few parsecs up to several hundred kilo-parsecs, exceeding the size of their host galaxy. The non-thermal emission related to the jets is associated to radio-loud AGN, and also used to explain the power-law shape of the X-ray flux. The formation mechanism of these jets is not well understood, and in fact, it is far from clear that jets are a common component to all AGN.

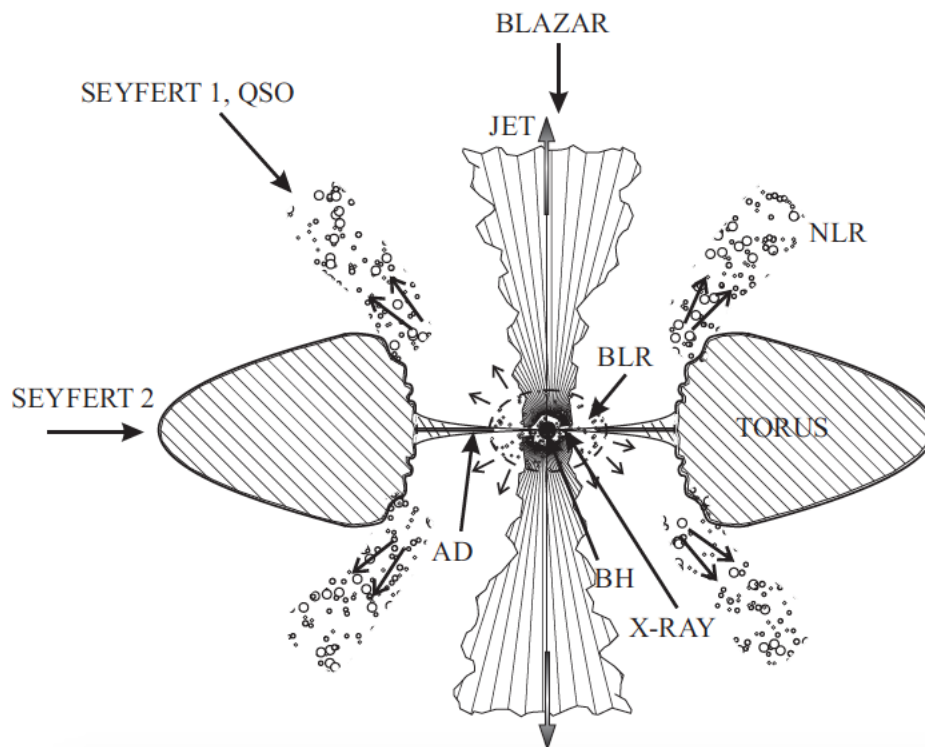


**Figure 2:** Schematic representation of the main components of an AGN according to unification models of AGN. Figure adapted from Jovanović et al. (2009).

## 1.2. Accretion

Since the discovery of the first Quasars in the 1960s, accretion onto a SMBH is believed to be the main source of energy powering these objects (Salpeter 1964; Zel'dovich 1964; Lynden-Bell 1969). Two main characteristics of QSOs lead to this assumption: the high redshifts at which they are observed, which implies high luminosities, and the rapid variability, which implies small sizes. We know today that the same mechanism powers also other less luminous classes of AGN, like Seyferts or LLAGN (see Section 1.1). Therefore, in this section, we will see in some detail the main aspects of the theory of accretion onto SMBHs.

Assuming a central accreting spherical body of mass  $M$  and radius  $R$ , the gravitational potential energy released by accretion of a mass  $m$  (falling free from infinity) onto its surface is:

$$\Delta E_{\text{acc}} = \frac{GMm}{R} \quad (1)$$

where  $G$  is the gravitational constant. If instead of for a single particle of mass  $m$ , accretion happens at a rate  $\dot{m}$  and all mechanical energy is eventually radiated, the resultant luminosity is given by:

$$L_{\text{acc}} = \frac{GM\dot{m}}{R} \quad (2)$$

where we see that for a given object with a given value of  $M/R$ , the accretion luminosity depends only on the *infall accretion rate* ( $\dot{m}$ ). Unlike other accreting objects like white dwarfs or neutron stars, black holes do not have a hard surface at a given radius  $R$ . Instead, there is a region at  $r < r_s$ <sup>4</sup> where matter could fall in without losing its mechanical energy, and therefore not contribute to the total radiated energy. This uncertainty is usually parametrised by the introduction of a dimensionless quantity  $\eta$ , the *efficiency*. Therefore, for the case which is relevant to this work, which is accretion onto a SMBH, equation 2 becomes:

$$L_{\text{acc}} = \frac{2\eta GM_{\text{BH}}\dot{m}}{r_s} = \eta \dot{m} c^2 \approx 5.7 \times 10^{46} \frac{\eta \dot{m}}{M_{\odot} \text{ yr}^{-1}} \text{ erg s}^{-1} \quad (3)$$

where  $M_{\text{BH}}$  is the mass of the central black hole. This equation shows that  $\eta$  measures how efficiently the rest mass of the accreting material is converted into radiation. Making a good estimation of  $\eta$  is a key ingredient of modelling accretion onto BHs, for which detailed calculations involving general relativity are needed, and the result depends on the exact geometry of the accretion flow. In general, a value of  $\eta \approx 0.1$  is usually assumed as the standard.

### 1.2.1. Eddington Limit

In this section we will derive an approximate theoretical upper limit for  $\dot{m}$ , the so-called *Eddington accretion rate* ( $\dot{m}_{\text{edd}}$ ). Taken from Chapter 1 of Frank et al. (2002). Some hypotheses are made for this derivation: *a)* steady (constant  $\dot{m}$ ) and spherically symmetric accretion flow, *b)* the accreting material is mainly fully ionised hydrogen and *c)* all accretion energy is converted into radiation. Under these circumstances, accretion can be halted if the accretion rate is high enough. Radiation emitted by the plasma which is closer to the central BH exerts an outward force on the infalling plasma at larger radii. This is due to Thomson scattering from that radiation on the free electrons<sup>5</sup>. If  $L_{\text{acc}}$  is the luminosity due to accretion (the only source

<sup>4</sup> $r_s = 2GM_{\text{BH}}/c^2$  is the Schwarzschild radius of a non-rotating BH.

<sup>5</sup>Protons are not taken into account for this radiation pressure, since the scattering cross-section for protons is a factor  $(m_e/m_p)^2$  smaller than that of electrons, with  $(m_e/m_p) \approx 5 \times 10^{-4}$

of luminosity in the case of accretion onto BHs) and  $\sigma_T = 6.7 \times 10^{-25} \text{ cm}^2$  the Thomson cross-section for electrons. The outward radial force exerted on a single electron at a distance  $r$  from the center of the BH is given by:

$$F_r = \frac{\sigma_T}{c} \frac{L_{\text{acc}}}{4\pi r^2} \quad (4)$$

where  $c$  is the speed of light. As the electrons are pushed out by the radiation, they drag the protons with them because of their mutual electromagnetic attraction. On the other hand, the gravitational force pushes these electron-proton pairs to the center with a strength:

$$F_g = \frac{GM_{\text{BH}}(m_p + m_e)}{r^2} \approx \frac{GM_{\text{BH}}m_p}{r^2} \quad (5)$$

The condition for radiation to be strong enough to stop accretion is that  $F_r \geq F_g$ , which implies:

$$L_{\text{acc}} \geq L_{\text{edd}} \equiv \frac{4\pi G m_p c}{\sigma_T} M_{\text{BH}} \approx 1.26 \times 10^{38} \left( \frac{M_{\text{BH}}}{M_{\odot}} \right) \text{ erg s}^{-1} \quad (6)$$

This equation defines the maximum luminosity of the central source, the *Eddington luminosity*, such that for  $L > L_{\text{edd}}$  the radiation pressure would exceed the inward gravitational attraction and accretion would stop. From equation 3 we have  $\dot{m} = L/\eta c^2$ , which means that the existence of a limiting luminosity implies also a limit on the steady accretion rate, the Eddington accretion rate:

$$\dot{m}_{\text{edd}} = \frac{L_{\text{edd}}}{\eta c^2} \approx 3.7 \times 10^{-8} \left( \frac{M_{\text{BH}}}{M_{\odot}} \right) M_{\odot} \text{ yr}^{-1} \quad (7)$$

where, for obtaining the numerical value on the right side of the equation we have used  $\eta = 0.06$ . From these numbers, we can see why accretion is a good candidate for powering AGN. For a typical AGN harbouring a SMBH of mass  $M \sim 10^8 M_{\odot}$ , from equations 6 and 7 we have  $L_{\text{edd}} \sim 10^{46} \text{ erg s}^{-1}$  and  $\dot{M}_{\text{edd}} \sim 4 M_{\odot} \text{ yr}^{-1}$ . Thus, powerful quasars like those seen at very high redshift can be sustained with just a few solar masses per year.

Note that because of the assumptions that were made for its derivation, we can only expect Eqs. 6 and 7 to be a first-order approximation. More realistic calculations depart from these values when the hypotheses are no longer valid, for instance with metallicity different to zero, non-spherical symmetry (e.g. a disc), variability (very common in AGN) or partly neutral gas. Despite this, it is common when talking about AGN to express the observed quantities in Eddington units ( $L/L_{\text{edd}}$  and  $\dot{m}/\dot{m}_{\text{edd}}$ ).

### 1.2.2. Accretion Discs

In a realistic situation, the infalling gas will have a non-zero angular momentum component, and will therefore orbit around the BH. The natural tendency of the accreting material is to concentrate in the equatorial plane, forming a thin accretion disc. [Shakura & Sunyaev \(1973\)](#) developed the classical theory of geometrically thin and optically thick accretion discs. The basic idea is that, because of viscosity, the angular momentum of the gas is transferred outward, allowing it to spiral further into the centre. During this process, a considerable fraction of the gravitational energy in the gas is converted into electromagnetic radiation, with a relatively high efficiency that depends on the BH spin. General relativity predicts the existence of an *innermost stable circular orbit* (ISCO) around a black hole, such that matter at radii below this ISCO cannot maintain its orbital motion and falls directly into the BH event horizon, without radiating

its remaining energy. Therefore, a larger ISCO implies a smaller efficiency, since less gravitational energy is extracted before the gas is advected. For a non-rotating (Schwarzschild) BH, general relativity predicts a value of  $6r_g$ <sup>6</sup> for the ISCO which in turn implies  $\eta = 0.057$ , while for a Kerr BH rotating at its maximum spin the ISCO approaches  $r_g$ , and  $\eta = 0.42$ . A value of  $\eta \approx 0.1$  is usually assumed as the standard. A more detailed explanation of this matter can be found in Chapter 3 of [Netzer \(2013\)](#).

The emitted spectrum of such a geometrically thin and optically thick accretion disc can be approximately calculated making a very simple assumption, namely, that the disc is composed of rings of infinitesimal radial thickness, each one emitting as a black body with different temperature  $T(R)$ . The integrated spectrum resulting from adding up all the individual contributions has the shape shown in Figure 3, and is characterised by a temperature:

$$T_* = \left( \frac{3GM_{\text{BH}}\dot{m}}{8\pi r_{\text{in}}^3 \sigma} \right)^{1/4} \quad (8)$$

where  $r_{\text{in}}$  is the innermost radius of the disc. The order of magnitude of  $T_*$  tells us where to expect the peak emission of the AD. For a typical disc in a luminous quasar, the peak emission of the disc falls in the UV/optical range (black line in Figure 3). This is an observed feature and is called the big blue bump. In contrast, for a truncated accretion disc (i.e.  $r_{\text{in}} < \text{ISCO}$ ), or one with a highly sub-Eddington accretion rate ( $\dot{m} \lesssim 10^{-3}\dot{m}_{\text{edd}}$ ), this peak is expected to be shifted towards lower energies/frequencies (yellow and red lines in Figure 3). We will see that both these scenarios are common in LLAGN.

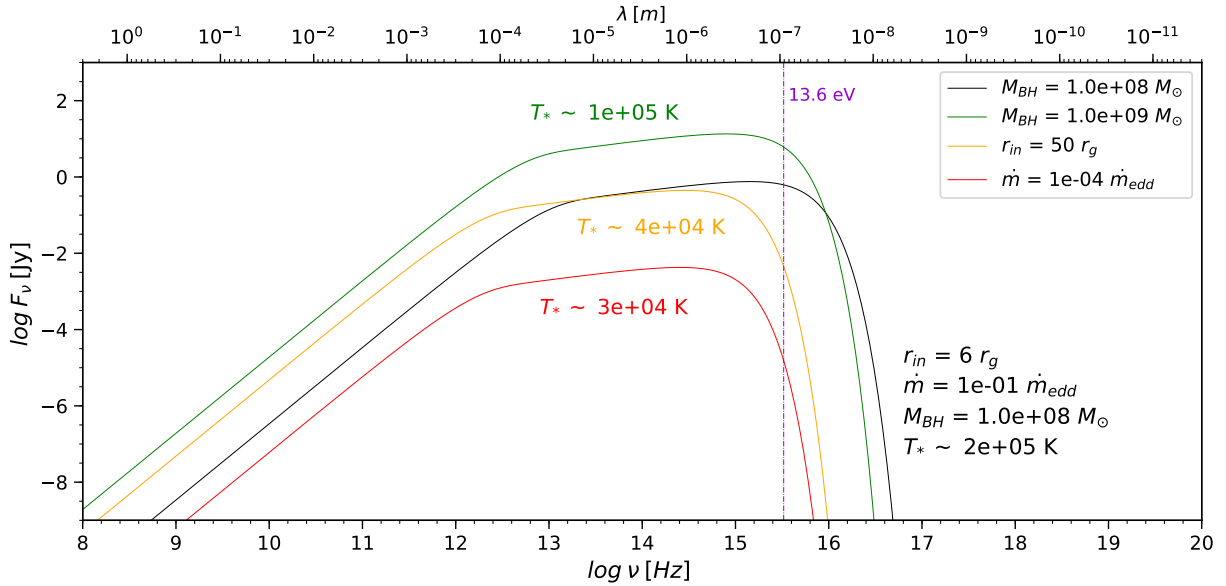


**Figure 3:** Emitted spectrum of a classical [Shakura & Sunyaev \(1973\)](#) slim accretion disc. The black line represents a standard disc reaching the ISCO. The parameters ( $r_{\text{in}}$ ,  $\dot{m}$  and  $M_{\text{BH}}$ ) are indicated in the figure. The other lines represent changes in one of these parameters, keeping the others fixed. The green line shows the effect of increasing the mass of black hole one order of magnitude. The yellow line corresponds to a truncated disc, and the red line to a disc with a very low accretion rate. The vertical purple line shows the ionisation potential of hydrogen. Note how both the truncated disc and the one with low accretion rate provide far less ionising photons than the standard disc. For all discs  $\eta = 0.06$  and  $r_{\text{out}} = 10^4 r_{\text{in}}$  was assumed.

<sup>6</sup> $r_g$  is the so-called gravitational radius,  $r_g = GM/c^2$



### 1.3. Low Luminosity AGN

In general, AGN spend most of their life-time in a low-luminosity state rather than in a quasar state. This makes *low-luminosity active galactic nuclei* (LLAGN) the most common population of active nuclei, including about one third of all galaxies in the local Universe (Ho 2008). As the name suggest, they are defined by its low bolometric luminosity ( $L_{\text{bol}} \lesssim 10^{42} \text{ erg s}^{-1}$ ,  $\log(L_{\text{bol}}/L_{\text{edd}}) \lesssim -3$ ), which is associated to low mass-accretion rates. Nevertheless, their observed spectra show some notable features which differentiate them from other AGN types, which suggests that LLAGN are not simply scaled-down versions of Seyferts; in fact, it is not clear at all whether the unification models described in Section 1.1.2 can properly describe these objects.

Figure 4 shows the averaged spectral energy distribution (SED) of 150 nearby type 1 AGN separated at four luminosity regimes (measured in Eddington ratio,  $L_{\text{bol}}/L_{\text{edd}}$ ). We will focus on two subsets: classical luminous AGN, with  $0.1 \leq L_{\text{bol}}/L_{\text{edd}} \leq 1$  (blue circles in Figure 4), and LLAGN, with  $L_{\text{bol}}/L_{\text{edd}} \leq 10^{-3}$  (orange squares). It can be seen that the main observational features separating these two classes are: *i*) the big blue bump ( $\log \nu \sim 10^5\text{--}10^9 \text{ Hz}$ ) which is the footprint of a standard slim accretion disc (Ho et al. 1996; Ho 1999) is absent for LLAGN. Instead, the peak emission appears in the mid-IR, forming a "big red bump"; *ii*) the optical/UV slope is much steeper in LLAGN; *iii*) there is no evidence of the soft X-ray excess, and *iv*) LLAGN appear to be radio-loud sources.

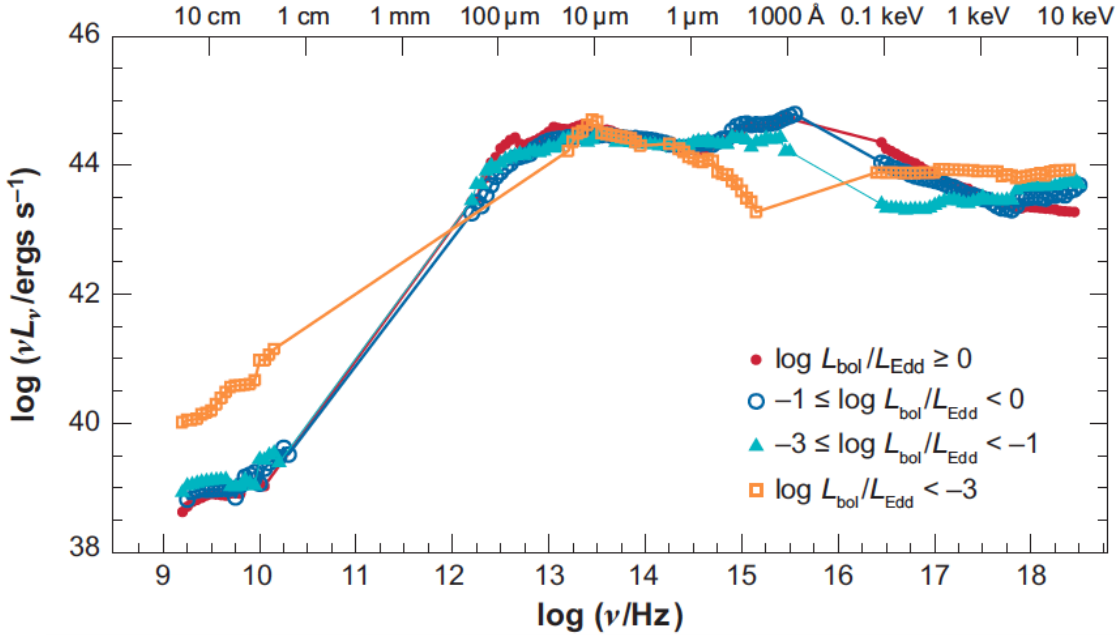


**Figure 4:** Composite SEDs of 150 nearby type 1 AGN binned by Eddington ratio. The sample spans 4 orders of magnitude in BH mass ( $M_{\text{BH}} \approx 10^5\text{--}10^9 M_{\odot}$ ) and 6.5 in Eddington ratio ( $\log(L_{\text{bol}}/L_{\text{edd}}) \approx 10^{-6}\text{--}10^{0.5}$ ). All SEDs are normalised at  $1 \mu\text{m}$ . There are significant differences separating the spectra of LLAGN (orange squares) from other more luminous AGN. Figure adapted from Ho (2008).

### 1.3.1. Accretion Flow at Low Accretion Rates

As already noted, there are multiple lines of both theoretical and observational evidence suggesting that LLAGN are not just scaled-down versions of more luminous AGN. At the low accretion rates characteristic of LLAGN ( $\dot{m} \lesssim 10^{-3} \dot{m}_{\text{edd}}$ ), structural changes that depart from the unification models are predicted to take place. The broad-line region and the torus are no longer supported by the radiation pressure from the nucleus (Nicastro et al. 2003; Elitzur & Ho 2009; Elitzur & Shlosman 2006). Moreover, the accretion flow becomes less dense and optically thin, and cannot cool efficiently. The geometrically thin and optically thick disc becomes unstable, and below a certain radius is replaced by a quasi-spherical hot flow, usually known as a *radiatively inefficient accretion flow* (RIAF; Quataert 2003). This scenario is suggested by the low Eddington ratios typical of LLAGN and their low inferred radiative efficiencies  $\eta$ , and is further supported by the apparent lack of big blue bump emission. The exact dynamics controlling RIAFs belong to an active research area, but they are believed to be dominated by advection, convection, or outflows.

An optically thick geometrically thin accretion disc can also exist, although due to the presence of the RIAF, it will be a truncated disc (Figure 5). The main effect of the truncation of the disc on its emitted spectrum is the shift towards lower frequencies of the emission peak (Figure 3). Hence, the mid-IR peak and the steep optical/UV continuum observed at the SEDs of many LLAGN further support the truncated disc hypothesis.

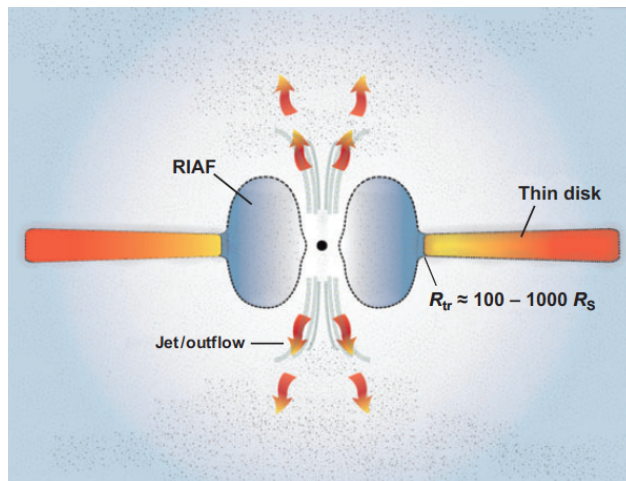


**Figure 5:** A diagram showing the structural changes predicted for low accretion rates, consisting of three components: an inner, radiatively inefficient accretion flow (RIAF); an outer, truncated thin disk; and a jet or outflow. Figure adapted from Ho (2008).

Finally, the radio-loudness typical of LLAGN suggests also the presence of a jet, i.e. collimated outflows of plasma accelerated at relativistic speeds along the axis of the system (Falcke & Markoff 2000; Markoff et al. 2005). The formation of the jet is still an open question, although it could be related to the RIAF itself: poloidal magnetic field components arising at RIAFs could channel charged particles into the polar regions, where the jet would be formed (Rees et al. 1982; Ballantyne 2007). The non-thermal emission related to these jets could be detected as synchrotron emission at radio frequencies and as inverse-Compton radiation in the X-ray.

Although the present discussion was made in the context of LLAGN, and therefore describes accretion onto supermassive black holes, there are indications that it can be extended to BHs over the entire mass



range, from stellar-mass BHs to SMBHs like Sgr A\* and LLAGN, as long as they are accreting at a very sub-Eddington rate. The so-called fundamental plane of black holes shows that there is a common correlation between the radio and the X-ray luminosity once the black hole mass is taken into account (Merloni et al. 2003; Falcke et al. 2004). This suggests that the same physical processes regulate the energy output in all these systems, namely, radiatively inefficient accretion flows and jet-activity.

### 1.3.2. The Ionising Continuum in LLAGN

Despite the theoretical models discussed in the previous section, there are still many open questions regarding the origin physical origin of LLAGN emitted spectrum. One big difficulty arises from the prediction that the accretion disc, if existing at all, must be truncated. If a truncated disc peaks on the mid-IR instead of the UV, what is then the exact shape of the ionising continuum (i.e.  $h\nu \geq 13.6$  eV,  $\lambda \leq 911$  Å) on these sources? And, which are the physical processes giving rise to that continuum?

There is a lack of consensus about the solution to these questions. High-angular resolution observations indicate that the ionising continuum can be an extension of the observed power-law shape due to self-absorbed synchrotron emission. Still, some authors argue that a radiatively efficient thin accretion disc may persist at low accretion rates, and therefore be present at LLAGN (Maoz 2007). In addition, ionisation models based on RIAFs (Yu et al. 2011) predict a very different continuum than those which are purely based on jets (Markoff et al. 2005; Prieto et al. 2016; Reb et al. 2018).

As already mentioned in Section 1.1.1, although the terms LINER and LLAGN refer to different categories, most LINERs are also LLAGN. Therefore, the open questions that remain on which are the main excitation mechanisms on LINERs are closely related to the present discussion. A wide variety of conjectures have been proposed about this topic. Some authors have attempted to explain the observed line ratios in LINERs by means of star-formation (Terlevich et al. 1992); shocks of different nature has also been proposed for this matter (Ho et al. 1993; Sugai & Malkan 2000). For some specific objects, like NGC 1052, there are more complex models which involve a combination of a small-scale turbulent accretion disc with jets and shocks (Dopita et al. 2015).

The biggest observational obstacle for checking the models and predictions discussed is that hydrogen absorption from the interstellar medium (ISM) makes it impossible to probe the ionising continuum shortwards of  $\lambda \sim 1000$  Å, which is precisely the spectral region where the emission from a disc would be expected to peak, and where the continuum becomes ionising.

## 1.4. Aim of this work

In the present work, we try to cast some light on the above mentioned open questions regarding LLAGN and LINERs. To that end, we use photoionisation simulations for a sample of LLAGN, and compare their output spectra with high-angular resolution observations of fine structure mid-IR lines in the same nuclei. This comparison is done via diagnostics diagrams, where two given pairs of line ratios are compared. The novelty of this study is that as an input for the photoionisation simulations, we use high-angular resolution spectral energy distributions (SEDs) across nearly the entire EM spectrum. Using these observations, we constrain the shape of the UV continuum emission up to the shorter wavelength possible, typically  $\sim 2000$  Å, and interpolate the ionising continuum between the UV and the X-ray assuming a power-law shape ( $F_\nu \sim \nu^{-\alpha}$ ). With this approach we aim to figure out whether the power-law interpolation is enough to reproduce the observed line ratios, or conversely, an additional contribution like that of an accretion disc is needed.

## 2. Dataset and Methodology

### 2.1. The Sample

The sample studied in this work consists of ten nearby LLAGN ( $D \lesssim 30\text{Mpc}$ ), nine of them being also LINERs. These galaxies have been selected because they represent the nearest known LLAGN. This allows the availability of high-angular resolution data from the HST in the optical range, and using adaptive optics and diffraction-limited imaging in the IR. Besides, some of these sources, like M87, NGC 1052 or the Sombrero Galaxy, are prototypical nuclei representing the LLAGN and LINER class. More detailed information about these galaxies can be found in Table 1.

Name	Type	Class	$z$	D [Mpc]	Ref.	FWHM [pc]	$1''$ [pc]	$A_V$ [mag]
NGC 404	LINER 2	SA(s)0	-0.000160	3.05	<a href="#">Dalcanton et al. (2009)</a>	1.2	14.8	0.160
NGC 4594 (M104)	LINER 2	SA(s)a	0.003416	9.08	<a href="#">Jensen et al. (2003)</a>	3.1	44.0	0.140
NGC 1097	LINER 1	SB(r'l)b	0.004240	14.2	<a href="#">Tully et al. (2009)</a>	8.9	68.8	0.073
NGC 1386	Sy 2	SB(s)a	0.002895	15.3	<a href="#">Jensen et al. (2003)</a>	6.7	74.2	0.034
M87 (3C274)	LINER 1	cD	0.004283	16.7	<a href="#">Blakeslee et al. (2009)</a>	9.2	81.0	0.063
NGC 4579 (M58)	LINER 1	SAB(rs)b	0.005060	16.7	<a href="#">Tully et al. (2013)</a>	6.3	81.0	0.112
NGC 1052	LINER 1.9	E4	0.005037	18.0	<a href="#">Jensen et al. (2003)</a>	10.5	87.3	0.073
NGC 3169	LINER 2	SA(s)a	0.004130	24.7	<a href="#">Mandel et al. (2009)</a>	10.9	119.7	0.085
NGC 4261 (3C270)	LINER 1h	E2-3	0.007378	32.4	<a href="#">Tully et al. (2013)</a>	12.3	157.1	0.049

**Table 1:** Sample of galaxies sorted by increasing distance. The spatial resolution is estimated as the FWHM of the most compact object found in the FOV. In all cases, the Galactic extinction has been corrected using the reddening values from [Schlafly & Finkbeiner \(2011\)](#) and the extinction curve from [Cardelli et al. \(1989\)](#).

### 2.2. High Angular Resolution SEDs

Unlike other types of active galactic nuclei, LLAGN are commonly outshined by their host galaxy. Therefore, very high-angular resolution datasets are needed in order to efficiently probe only the nuclear region and avoid as much contamination as possible from stellar activity. Figure 6 gives a clear example of this. There are obvious differences between the high and low resolution data sets, especially in the visible/UV range, where the low resolution flux is about 2 orders of magnitude larger. Besides this, even though we are especially interested in the ionising part of the spectrum ( $\lambda < 911 \text{ \AA}$ ), our datasets must include observations across the whole electromagnetic spectrum whenever possible, in order to have a general picture of the mechanisms going on at these nuclei. This also allows us to check for variability at different spectral ranges.

Next, we shortly discuss, from longer to shorter wavelength, the origin of these data. Radio and microwave measurements mainly come from the Very Large Array (VLA), the Very Long Baseline Interferometry (VLBI), and the Atacama Large Millimeter/submillimeter Array (ALMA). The high baselines allowed by these interferometers provide some of the highest spatial resolution ( $\sim 0.1''$ ). In the IR we include observations that use adaptive optics in the near-IR (NACO) and diffraction-limited imaging in the mid-IR (VISIR). Both these instruments are part of the Very Large Telescope (VLT) and also provide sub-arcsec ( $\lesssim 0.4''$ ) resolution. In the visible/UV archival data of highest resolution available from the Hubble Space Telescope (HST) complement the observations. Nuclear fluxes are measured using aperture photometry of the unresolved central component by subtracting the local background from an annulus. Lastly, X-ray flux measurements from Chandra, XMM-Newton, Integral, and NuSTAR have been collected by an extensive and careful search in the literature. Despite their lower spatial resolution, they can consistently be compared to sub-arcsec

measurements at other frequencies, since the high energy flux is dominated by the nucleus with negligible contribution from the host galaxy.

All these data were compiled and extracted within the framework of the PARSEC project, and can be found in the works of Fernández-Ontiveros, Juan Antonio et al. (2013); Reunanen et al. (2010); Prieto et al. (2010).

### 2.3. Emission-line spectrum

In addition to the above described datasets, high-angular resolution observations of emission line fluxes are also crucial for this work. These data come from the Infrared Spectrograph (IRS) on board of Spitzer, and have been collected from the Cornell Atlas of Spitzer/Infrared Spectrograph Sources (CASSIS; Lebouteiller et al. 2015). One example of such an emission-line spectrum can be seen in Figure 7. All the lines used for this work are collisionally excited fine-structure lines which lie on the mid-IR range, e.g. [Ne II]12.8  $\mu\text{m}$  or [O IV]25.9  $\mu\text{m}$ .

For each line, the total flux is calculated via direct numerical integration, but also with a gaussian model fit. Only in one case, the flux is taken from the gaussian fit, namely the [Ne II]12.8  $\mu\text{m}$  line in NGC 1097. This is done to avoid contamination from a PAH (Polycyclic Aromatic Hydrocarbon) whose emission lies next to the base of this line. The PAH is probably associated with the formation ring (Prieto et al. 2019) which is near the nucleus of this galaxy (Fig. 8, left panel). It can be seen that the short slit (SH) from the IRS includes partially the star-forming ring (Fig. 8, right panel), which explains this contamination. This ring is also probably contributing to the [Ne II]12.8  $\mu\text{m}$  flux, which must be taken into account when analysing the obtained results.

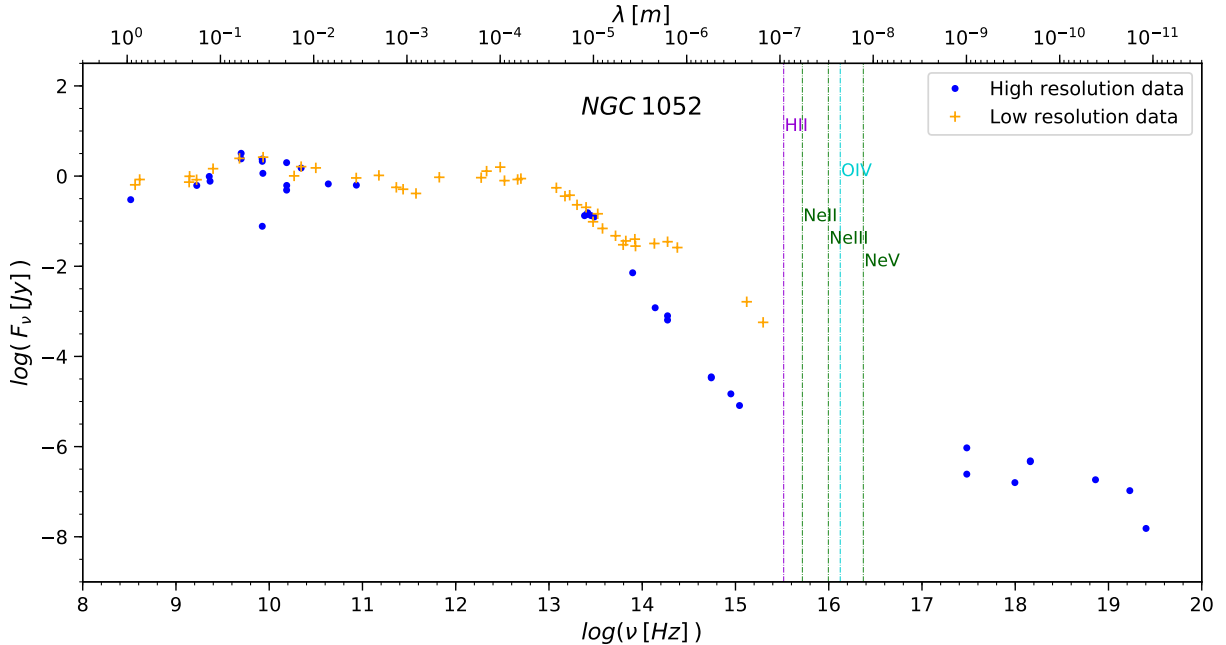


**Figure 6:** Spectral flux distribution for the nucleus of NGC 1052. High and low-angular resolution data are represented by blue dots and orange crosses respectively. Vertical coloured lines are drawn at the ionisation potential of some representative species.

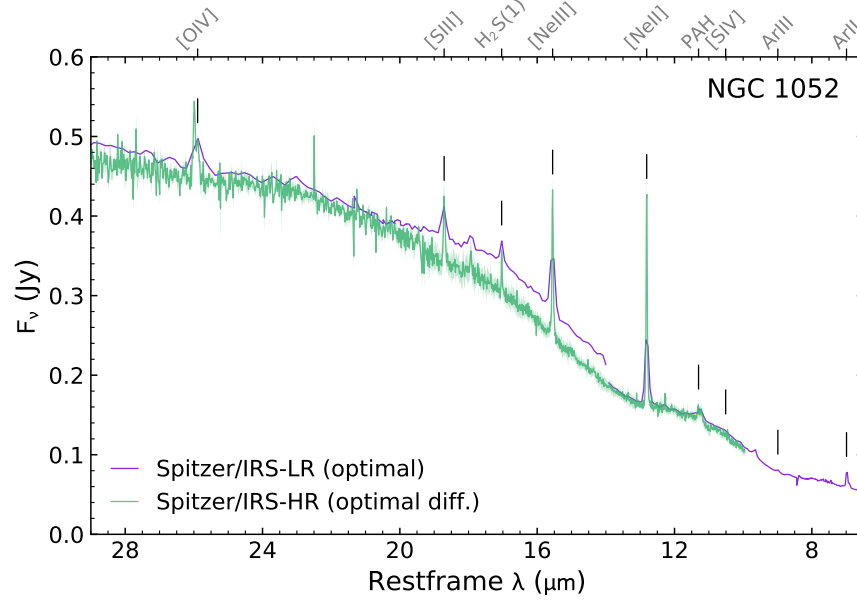


**Figure 7:** Example spectrum from the IRS spectrograph at high- and low-spectral resolution for the nucleus of NGC 1052, showing some of the fine-structure lines used in this work. Note the prominent [Ne II] and [Ne III] lines. (Courtesy of J.A. Fernández Ontiveros).

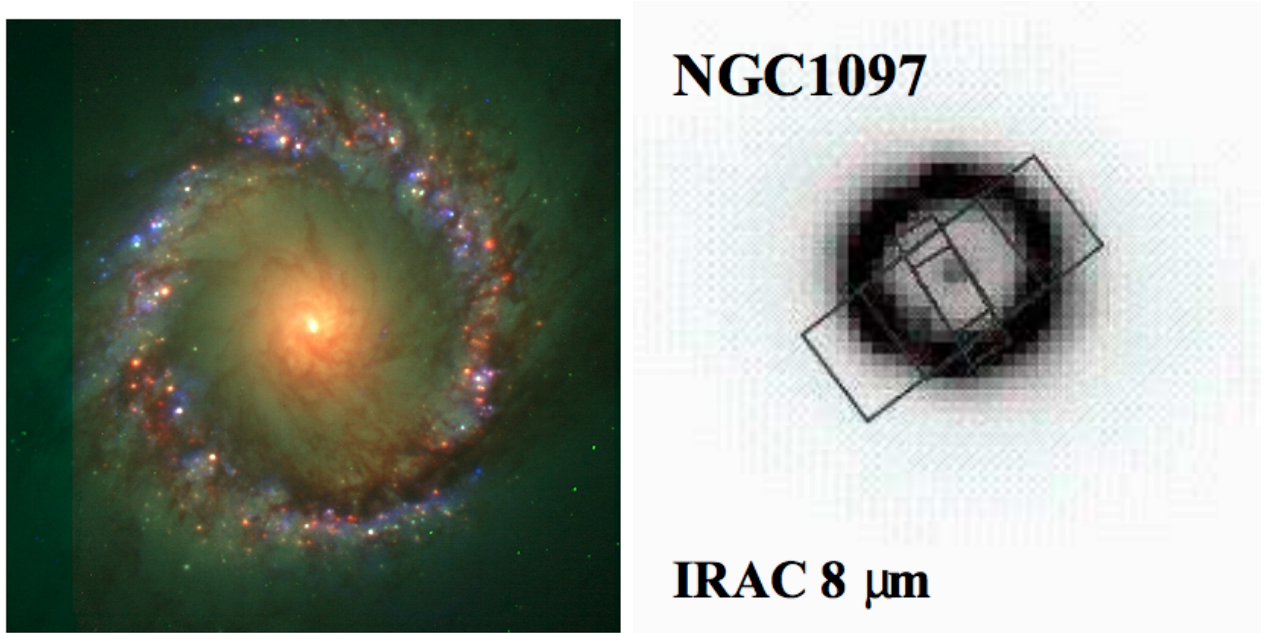


**Figure 8:** *Left panel:* the nucleus of NGC 1097 and the star-forming ring around it. Composition of different images from the HST in V and I bands, and from VLT/NACO in the K band. FOV  $\approx 30'' \times 30''$ . (Courtesy of J.A. Fernández Ontiveros). *Right panel:* IRAC 8  $\mu\text{m}$  image of NGC 1097 with the SH (Short-High) and LH (Long-High) slits overlaid. These are the two high-resolution slits of the IRS. The SH slit covers the 9.9–19.5  $\mu\text{m}$  range, and the LH slit covers 18.8–37.1  $\mu\text{m}$  range. It can be seen that even the SH slit includes partially the star-forming ring, which causes contamination in the [Ne II] 12.8  $\mu\text{m}$  line for this nucleus. Note also that, at the wavelength of this image, the disc clearly outshines the nucleus. Figure adapted from [Bernard-Salas et al. \(2009\)](#).

Using the IR band for probing the emission-line spectrum has some advantages: IR lines correspond generally to lower-energy atomic transitions compared to optical lines, which means that they require less energetic collisions, and therefore less global temperature. This is crucial for the low luminosity objects we are studying. Also, the IR is less absorbed by dust.

## 2.4. Methodology

The overall method followed in this work is as follows: first, the high-angular resolution SEDs above described are fitted using a given model, which for the most of this work is a combination of broken power laws ( $F_\nu \sim \nu^{-\alpha}$ ) plus a truncated accretion disc. Then, using these models as input radiation field in the photoionisation code `CLOUDY`, we construct photoionisation models whose predicted line ratios can be compared with high-angular resolution observations.

### 2.4.1. Fitting the SEDs

The high-resolution SEDs presented in section 2.2 have been fitted to broken power laws of the form  $F_\nu \sim \nu^{-\alpha}$ , with a different spectral index  $\alpha$  in each spectral range: from the radio to the infrared, from the IR to the UV, and from UV to X-rays. These power laws become straight lines of slope  $-\alpha$  when the flux/energy distributions are plotted in log-log form, which is the case trough all this work. The fits are tuned manually, changing the slope and the y-intercept of the lines based on two criteria: *a)* the fits must represent the high-resolution continuum in all spectral ranges, but especially in the UV and the X-ray, since this is where the continuum becomes ionising, and therefore the photoionisation models are most sensitive to this range. *b)* Whenever possible, the broken power laws have been forced to meet at the breaking frequency, i.e. the frequency at which the spectral index changes. On top of that, a simulated truncated accretion disc is added. The defining parameters of each disc (accretion rate and truncation radius) are adjusted so that it represents the brightest disc congruent with the data.

This process is applied to 4 LLAGN of our sample, namely NGC 1052, NGC 4594, NGC 1097 and M87. Additionally, the same analysis is repeated for the quasar 3C273, one of the best known AGN, which clearly exhibits the blue bump characteristic of luminous accretion disc. This allows us to compare LLAGN as a class to classical a luminous AGN.

For some objects, we have also used a more complex model, which simulates the spectrum emitted by a compact jet. A more detailed description of this model can be found in [Markoff et al. \(2008\)](#).

### 2.4.2. Photoionisation Simulations

All the photoionisation models computed for this work have been made using `CLOUDY`. `CLOUDY` is an open-source software which simulates the physical conditions within a non-equilibrium gas cloud exposed to an external source of radiation, and predicts the thermal, ionisation, and chemical structure of this cloud, and well as its emitted spectrum. It makes so by solving the equations of statistical equilibrium, charge conservation, and conservation of energy.

`CLOUDY` needs some inputs to perform these calculations, among which especially relevant is the incident radiation field (the source of ionisation), for which we use the fits described in Section 2.4.1. Other properties of the cloud must be specified, like its density, composition and geometry. For all the models described in this work, these properties have been defined as follows: regarding chemical composition, solar metallicity is assumed, and Polycyclic Aromatic Hydrocarbons (PAHs) are included. The assumed geometry is spherical,

at a distance  $r_0$  from the source. CLOUDY uses the total hydrogen density (the sum of the protons in atomic, ionic, and molecular form) as the cloud density. In all our modes we are giving typical values of  $1 \lesssim \log(n(\text{H})) \lesssim 5 \text{ cm}^{-3}$ . The total pressure<sup>7</sup> is kept constant through the cloud, which forces the density to vary with radius. Therefore, the density value which is given as an input corresponds to  $n(\text{H})$  at the illuminated face of the cloud. Another important input for the models is the ionisation parameter  $U$ . This is the dimensionless ratio of hydrogen-ionising photons to total hydrogen density:

$$U = \frac{Q(\text{H})}{4\pi r_0^2 n(\text{H})c} \equiv \frac{\Phi(\text{H})}{n(\text{H})c} \quad (9)$$

where  $r_0$  is the distance between the centre of the radiation source and the illuminated face of the cloud,  $Q(\text{H}) [\text{s}^{-1}]$  is the number of hydrogen-ionising photons emitted by the central object, and  $\Phi(\text{H}) [\text{cm}^{-2}\text{s}^{-1}]$  is the surface flux of ionizing photons. Typical values for our models are  $-3.5 \lesssim \log(U) \lesssim -1$ .

Finally, the code also needs one or more stopping conditions, so it will stop the calculation whenever one of them is fulfilled. In our case we use hydrogen column density  $N(\text{H}) = 23 \text{ cm}^{-2}$  as an upper limit. This is equivalent to setting an outer radius for the cloud.

The version of CLOUDY used in this work is C17.01, described in [Ferland et al. \(2017\)](#).

---

<sup>7</sup>In the most general case, this includes pressure terms from thermal gas motions, turbulent motions, a magnetic field, the nearly isotropic radiation pressure produced by trapped emission lines, and the outward push of the incident radiation field on the gas



### 3. Results

We applied the methods described in Section 2.4 to our sample of LLAGN. In Section 3.1 the general shape of the high-angular resolution SEDs is described and compared to the low-angular resolution data. In Section 3.2 and 3.3 we compute photoionisation models at which the ionisation continuum is a combination of a power-law fit to the high-resolution data and a simulated accretion disc. In Section 3.4 a compact jet model, with an emission dominated by self-absorbed synchrotron plus inverse Compton, is used to compute the photoionisation models. Finally, in Section 3.5 we analyse the contribution of the accretion disc to the total ionisation in the LLAGN from our sample. For comparison purposes, in all sections a similar analysis has been carried out for the classical quasar 3C 273, one of the best known AGN and the first one to be discovered.

#### 3.1. The continuum shape at high-angular resolution

The high-resolution spectral flux distributions shown in the above panel of Figures 10, 11, 12, and 13 reveal an overall similar shape for all the studied LLAGN. These objects appear to be radio-loud, with a relatively flat flux distribution over several orders of magnitude at low energies. From the IR to the UV ranges, the flux shows a steep decrease. The X-ray data suggest that there is another turnover somewhere between the UV and the X-rays, and the continuum becomes less steep again. In contrast, the low-resolution data show clear bumps in the visible range, which can be associated with stellar activity.

One notable exception is NGC 404, whose spectral flux distribution is shown in Figure 9. In this case, the high-angular resolution data seem to be dominated by stellar activity in the visible range, as can be deduced by the similarity of the high and low-resolution data. Furthermore, the X-ray and radio luminosities, when compared to the optical luminosity, appear to be lower than in other LLAGN.

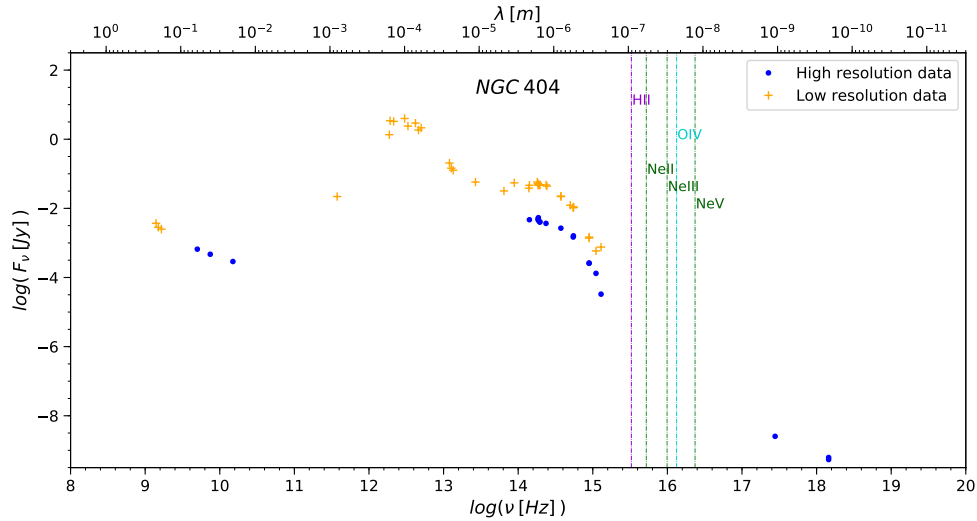


**Figure 9:** Spectral flux distribution of the nucleus of NGC 404. The similarity between the high and low-resolution data, both in shape and in magnitude, suggests that the high-angular resolution flux of this LLAGN is dominated by stellar activity. The vertical dashed coloured lines indicate the ionisation energy of some ionic species.

### 3.2. Power law + Accretion disc models

Figures 10, 11, 12, 13, and 14 show the modelled power laws and accretion discs for the LLAGN NGC 1052, the Sombrero Galaxy (NGC 4594), M87 and NGC 1097, and the Quasar 3C 273, following the method described in Section 2.4.1. The vertical dashed coloured lines indicate the ionisation energy of  $H^0$  (13.6 eV),  $Ne^0$  (21.6 eV),  $Ne^+$  (41.0 eV),  $Ne^{3+}$  (97.1 eV) and  $O^{2+}$  (54.9 eV). The name next to each vertical dashed line corresponds to the ionic species that can be produced by photons more energetic than this threshold. The power law spectral index  $\alpha$  for the optical/UV and X-ray ranges are written in the legend of each plot. Each figure also shows the main parameters which define the accretion disc, namely the inner radius ( $r_{in}$ , in units of  $r_g$ ), the accretion rate ( $\dot{m}$ , in units of  $\dot{m}_{edd}$ ) and the mass of the central BH ( $M_{BH}$ , in solar masses). This information is also listed in Table 2. The temperature  $T_*$  is also shown in each plot, although this is not a free parameter, but it is determined by the previous three parameters (equation 8). Table 2 also shows a 'normalisation factor' for  $F_\nu$ . The continuum flux of the accretion disc component is normalised by this factor in order to reproduce the data. This normalisation accounts for unknown uncertainties, like the error in  $M_{BH}$ , or the efficiency of some processes which depart from a canonical Shakura-Sunyaev disc.

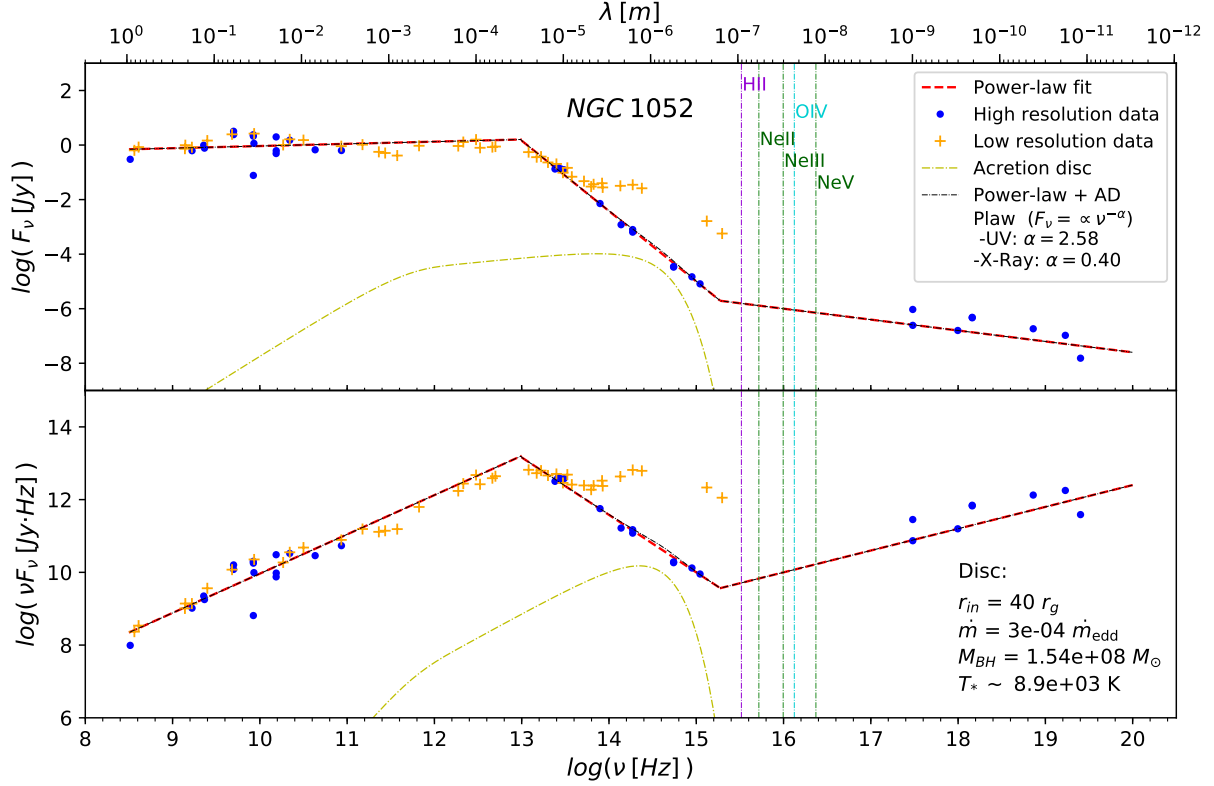
Overall, the spectral indexes of the fitted power laws for the LLAGN are in the interval  $-0.08 < \alpha < 0.26$  for the radio,  $1.20 < \alpha < 2.58$  for the IR/UV range, and  $0.40 < \alpha < 0.46$  (except for M87, with  $\alpha = 1.2$ ) in the X-ray.

Name	Disc			norm $F_\nu$	Power law spectral index $\alpha$			Type
	$r_{in}$ [ $r_g$ ]	$\dot{m}$ $\dot{m}_{edd}$	$M_{BH}$ $M_\odot$		Radio	Visible/UV	X-ray	
NGC 1052	40	$3 \times 10^{-4}$	$1.54 \times 10^8$	0.01	-0.08	2.58	0.40	LLAGN
NGC 4594	10	$3 \times 10^{-5}$	$1 \times 10^9$	0.01	-0.27	1.82	0.46	LLAGN
NGC 1097	50	$3 \times 10^{-3}$	$1.28 \times 10^8$	0.01	-0.002	1.70	0.40	LLAGN
M87	10	$5 \times 10^{-5}$	$6.4 \times 10^9$	0.005	0.26	1.20	1.20	LLAGN
3C 273	6	0.2	$7 \times 10^8$	1	0.58	0.58	1.60	Quasar

**Table 2:** Main defining parameters of the broken power laws and accretion discs, namely the truncation radius ( $r_{in}$ ), accretion rate ( $\dot{m}$ ), normalisation factor for the disc flux, and spectral index of the power law at the different spectral ranges. The classification of each AGN is also shown. References for  $M_{BH}$ : NGC 1052 (Woo & Urry 2002), NGC 4594 (Kormendy et al. 1996), NGC 1097 (van de Ven & Fathi 2010), M87 (Gebhardt & Thomas 2009), 3C 273 (Zu et al. 2011).

Figures 15, 16, 17, 18, and 19 show the line ratios diagnostics diagrams comparing the predictions from our photoionisation simulations with high-angular observations. Specifically, we show the  $[N III]15.6 \mu m / [N II]12.8 \mu m$  versus  $[O IV]25.9 \mu m / [N II]12.8 \mu m$  and the  $[N III]15.6 \mu m / [N II]12.8 \mu m$  versus  $[O IV]25.9 \mu m / [N III]15.6 \mu m$  diagrams. The black dots indicate the observed flux ratios with their associated uncertainty, and some particular LLAGN are marked with coloured dots. The green grid shows the model predicted line ratios for different values of the ionisation parameter  $U$  and the hydrogen density  $n$  in the initial step of the simulation. The input radiation field adopted for these models corresponds to the power-law plus accretion disc model shown in the figures above. The blue grid represents the model predictions using as input radiation field the 3C 273 continuum distribution shown in Figure 14. This allows us to compare the results from each LLAGN with those of an AGN powered by a prominent accretion disc in its continuum distribution.

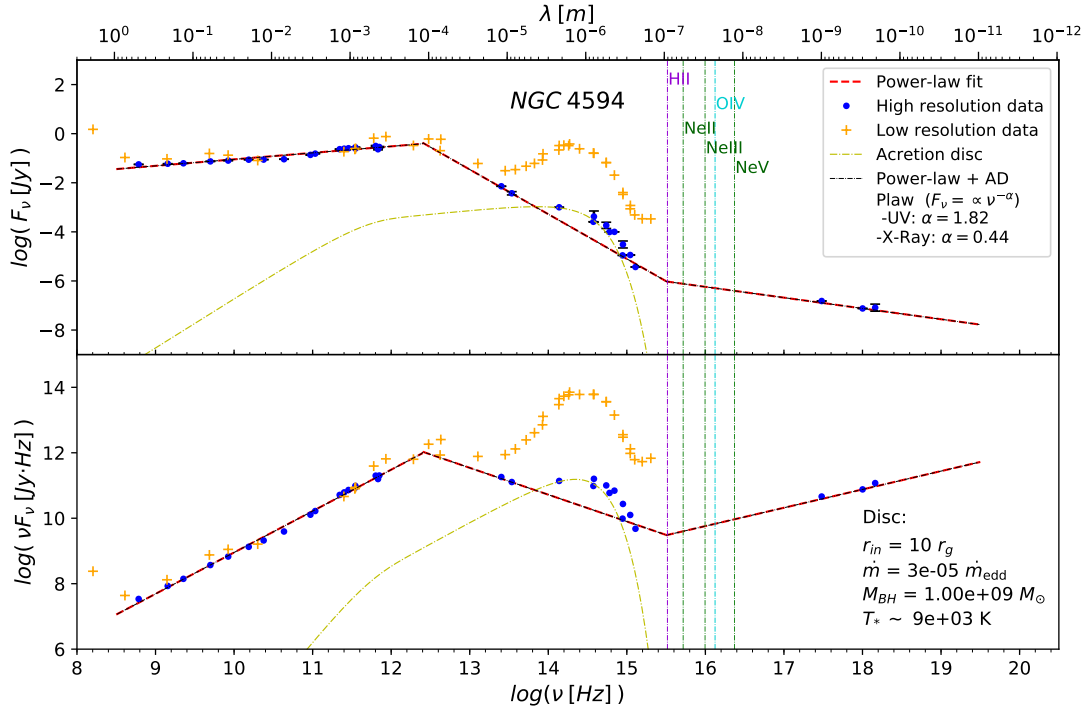




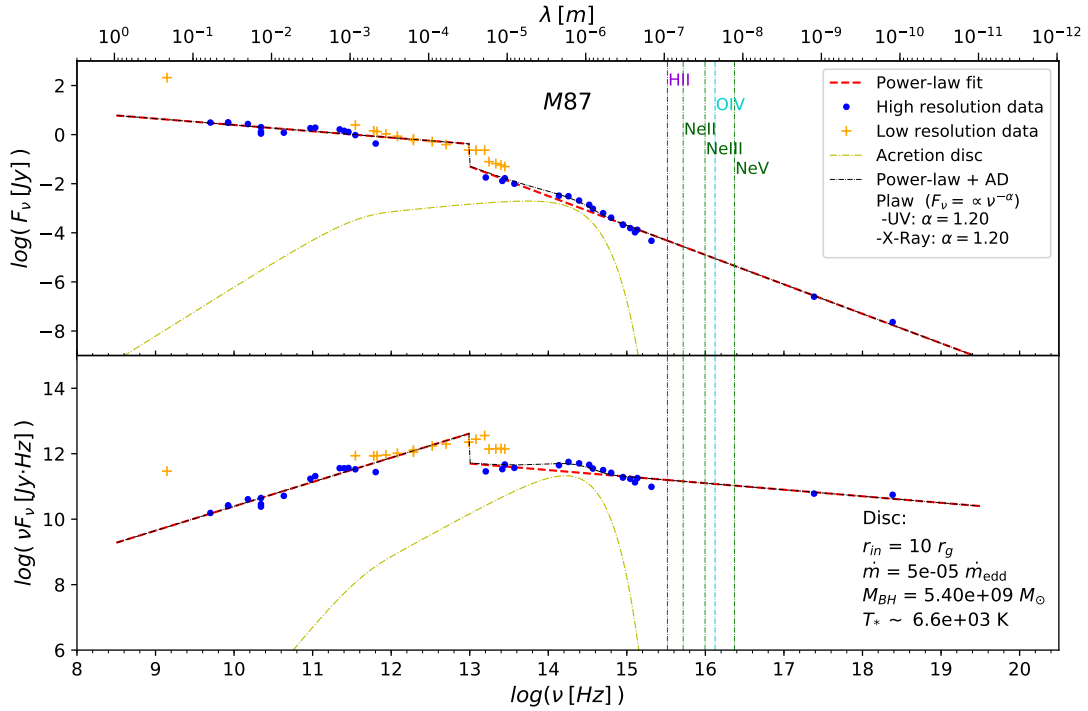
**Figure 10:** Power-law fit to NGC 1052. The blue dots and the orange crosses correspond to high and low-angular resolution data respectively. The red dashed line shows the broken power law; the associated spectral indexes are written in the legend. The yellow dashed line shows the contribution of the simulated accretion disc, whose defining parameters are plotted in the figure. The black dashed line represents the added contribution of the accretion disc and the power law. Vertical coloured lines mark the ionisation energy of the ionic species used in the diagnostics diagrams. The same data and fits are plotted in spectral flux (up) and spectral energy (down).

Looking at the diagnostics diagrams (e.g. Figure 15) it is visible that the ratios  $[\text{O IV}]/[\text{N II}]$  and  $[\text{O IV}]/[\text{N III}]$  lie in the range 0.1–1 for most LLAGN, with a few exceptions. NGC 1386 exhibits larger values for these ratios, comparable to those of the quasar 3C 273 ( $[\text{O IV}]/[\text{N II}] \sim 10$  and  $[\text{O IV}]/[\text{N III}] \sim 2$ ). NGC 1097 shows a similar deviation in the  $[\text{O IV}]/[\text{N III}]$  ratio. The other exception is NGC 404, although for this LLAGN we only have an upper limit for the  $[\text{O IV}]$  line. The ratio  $[\text{N III}]/[\text{N II}]$  is also in the range 0.1–1 except for NGC 1386, again with a similar value to that of 3C 273 ( $[\text{N III}]/[\text{N II}] \sim 4$ ).

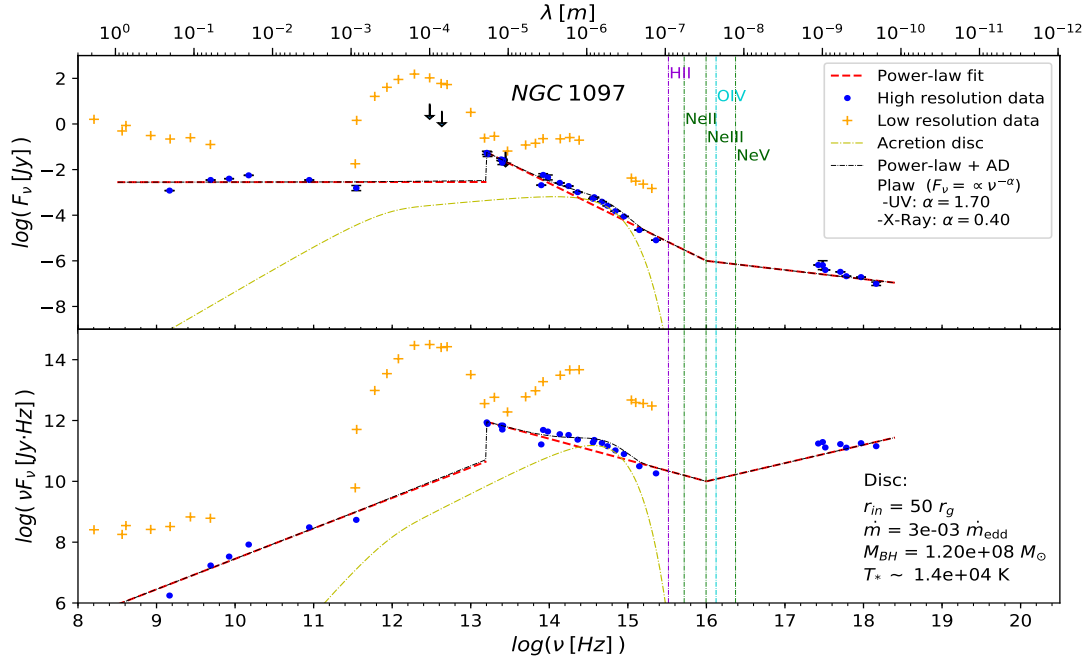
In general, the photoionisation models reproduce the observed data for values of  $n \sim 10^2\text{--}10^4$  and  $U \sim 10^{-2}\text{--}10^{-3}$ . However, for some objects (NGC 1386, NGC 1097 and NGC 404) any model from the LLAGN can properly reproduce its observations regardless of the value of  $n$  or  $U$ .



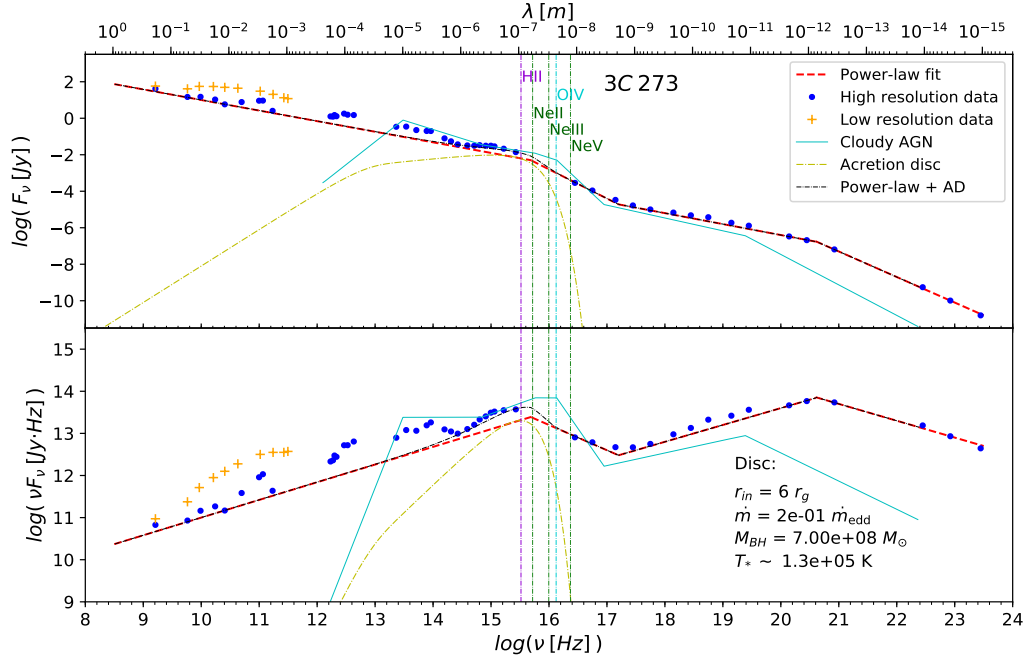
**Figure 11:** Power-law fit to NGC 4594. See caption of Figure 10 for details.



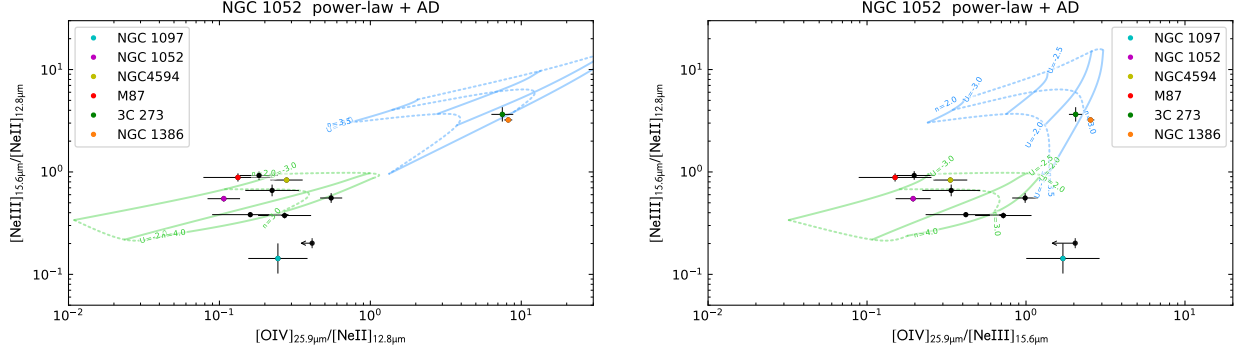
**Figure 12:** Power-law fit to M87. See caption of Figure 10 for details.



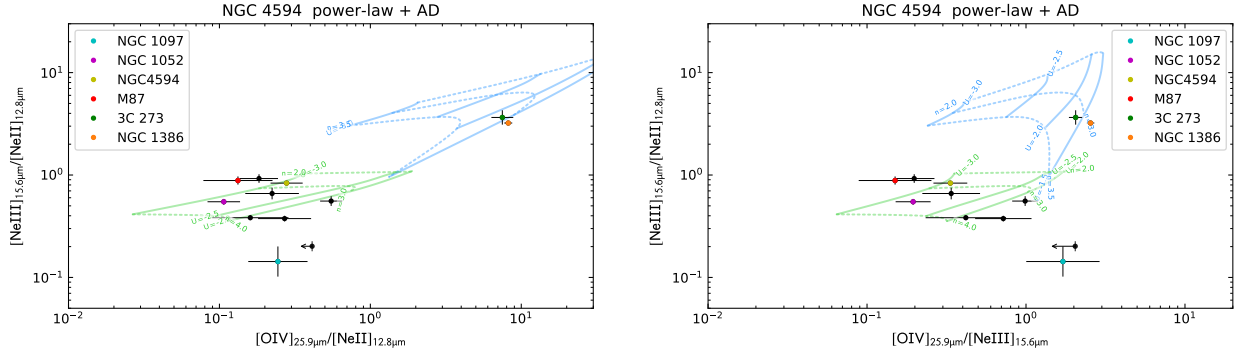
**Figure 13:** Power-law fit to NGC 1097. See caption of Figure 10 for details.



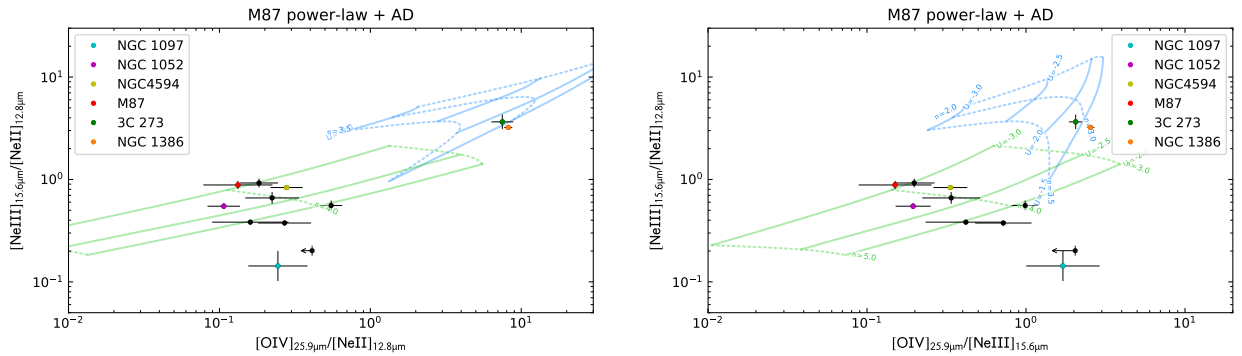
**Figure 14:** Power-law fit to 3C 273. The blue solid line represents the continuum derived by Mathews & Ferland (1987). This continuum is the standard Cloudy template for a radio quiet AGN, widely used in the literature. See caption of Figure 10 for additional details.



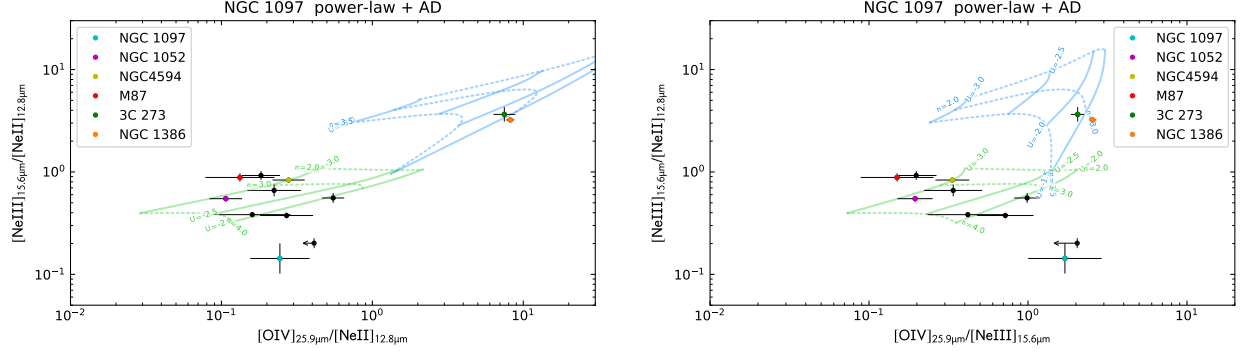
**Figure 15:** Diagnostics diagrams for the LLAGN sample with the NGC 1052 photoionisation model overlaid. Black and coloured dots show the observed flux ratios with their associated uncertainty. The green grid shows the values of line ratios which correspond to the CLOUDY simulations, for different values of ionisation parameter  $U$  and hydrogen density  $n$ . The input radiation field for these models is the power law plus accretion disc model shown above. The blue grid represents the model predictions using the 3C 273 power-law fit shown in Figure 14 as input radiation source.



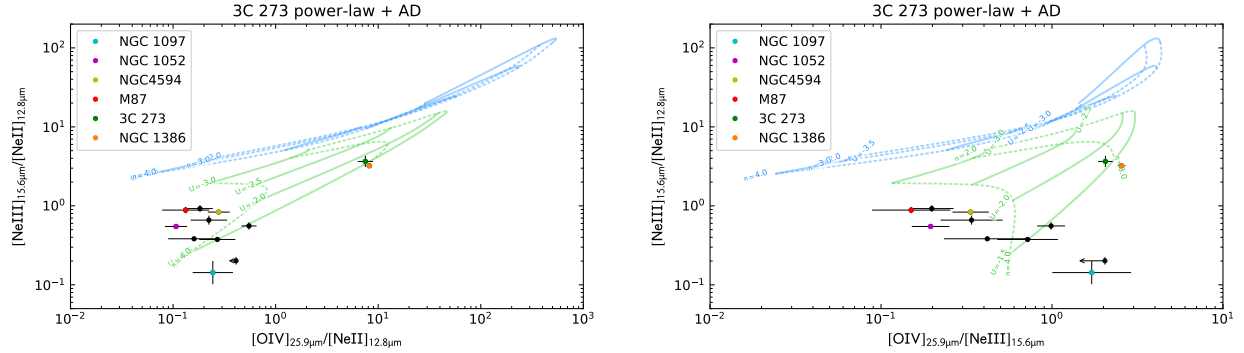
**Figure 16:** Diagnostics diagrams for the LLAGN sample with the NGC 4594 photoionisation model overlaid. See caption of Figure 15 for details.



**Figure 17:** Diagnostics diagrams for the LLAGN sample with the M87 photoionisation model overlaid. See caption of Figure 15 for details.



**Figure 18:** Diagnostics diagrams for the LLAGN sample with the NGC 1097 photoionisation model overlaid. See caption of Figure 15 for details.



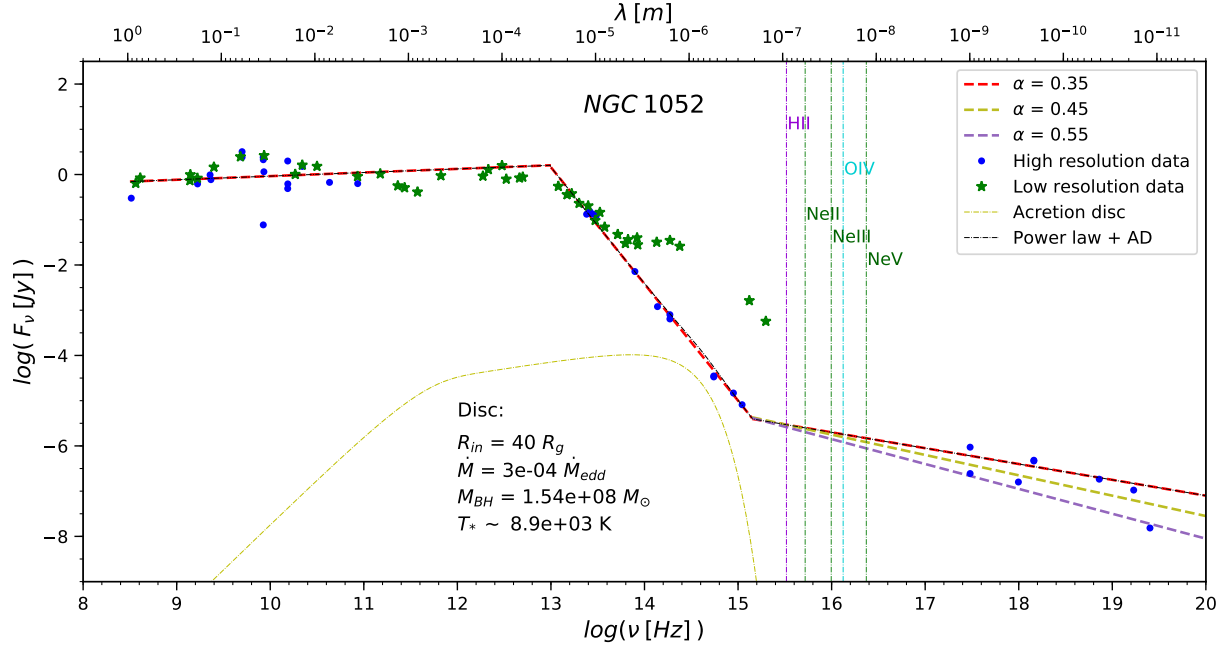
**Figure 19:** Diagnostics diagrams for the LLAGN sample with the 3C 273 photoionisation model overlaid. Unlike for the above shown diagrams, the blue grid shows the photoionisation models using CLOUDY’s standard AGN template as ionising radiation source. See caption of Figure 15 for further details.

Figure 19 shows that the line ratios of classical luminous AGN like 3C 273 are better reproduced by the power-law fit to its own SED rather than by the standard AGN template of CLOUDY. Also, note that these models approach the ratios of the LLAGN as the ionisation parameter decreases and the density increases.

### 3.3. Dependence with the spectral index

Due to dispersion in the X-ray flux observations, and especially, the fact that we are missing the information on the shape of the spectra between the UV and the X-ray, the power law corresponding to that spectral interval is not well constrained. This is an important point, as this range is precisely the ionising part of the spectrum. In this section we investigate the effect of possible uncertainties in the slope of the UV to X-ray continuum on the diagnostics diagrams. For this purpose, we made three different fits for different values of the spectral index:  $\alpha = 0.35, 0.45$  and  $0.55$ . The resultant fits are shown in Figure 20. For the CLOUDY models we kept  $\log(n/\text{cm}^{-3}) = 3$  in all cases, changing the ionisation parameter to sample the green grid in Figure 21.

In this case, the grid of photoionisation models do not cover all the observed ratios, although it lies in the same region where most LLAGN also are. It can be seen that as the ionising spectrum becomes steeper (i.e. a higher  $\alpha$  value), the photoionisation models move towards the AGN models.



**Figure 20:** Three different power-law fits to the X-ray flux spectrum, all coherent with the data. See caption of Figure 10 for other details.

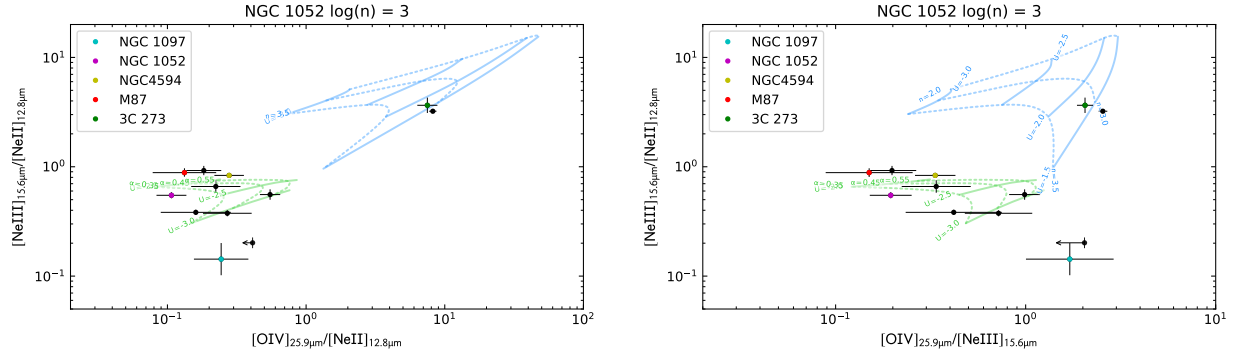


**Figure 21:** Diagnostics diagrams for the LLAGN sample overlaying three photoionisation models for NGC 1052 with different spectral index. See caption of Figure 15 for details.

### 3.4. Jet Model Comparison

The characteristic flat-to-inverted shape seen at the studied spectral flux distributions is very similar to that produced by self-absorbed synchrotron emission, i.e. the signature of strong non-thermal radiation produced by a compact jet (Blandford & Königl 1979). Therefore, in this section we will compute new photoionisation simulations using a more sophisticated and physically motivated model developed by Markoff et al. (2005) as input ionisation source. As described in Section 2.4, we introduced the continuum generated by this model into CLOUDY and compare its predicted line ratios with observations. The model consists of a compact jet and truncated accretion disc. Briefly, it simulates the following physical processes: hot particles are injected into the base of the jet, where thermal electrons produce synchrotron emission. The synchrotron photons

themselves interact with the electrons, producing inverse Compton emission, a process called synchrotron self Comptonisation (SSC). There is a shock point at the base of the jet where the electrons are accelerated into a power law energy distribution, which is maintained along the jet. Additionally the model includes a thin truncated accretion disc. This model has been used to reproduce the overall continuum emission of LLAGN (e.g. M81 in [Markoff et al. 2008](#)), including M87 ([Prieto et al. 2016](#)), NGC 1052 ([Reb et al. 2018](#)), NGC 1097 and NGC 4594 (L. Reb, priv. communication) in our sample.

Figures 22, 23 and 24 show the continuum predicted by this model for three of the objects we are studying, NGC 1052, NGC 1097 and the Sombrero galaxy. The continuum emission of this model is actually the sum of different components, including two synchrotron components, a truncated accretion disc and an inverse Compton components which dominates for high energies. Here we are plotting the inverse Compton component together with each jet. The contribution of the other components in the case of NGC 1052 can be seen in Figure 1 of [Reb et al. \(2018\)](#). The power law models shown in section 3.2 are also plotted for comparison.

The diagnostics diagrams shown in Figures 25, 26 and 27 show that these photoionisation models can reproduce the observed line ratios, when they are computes for the same range of ionisation parameter and density as the previous power-law models ( $10^{-2} < U < 10^{-3}$  and  $10^2 < n < 10^4$ ). Just as with those models, there are three LLAGN which are nor reproduced by any model, namely NGC 1097, NGC 1386 and NGC 404.

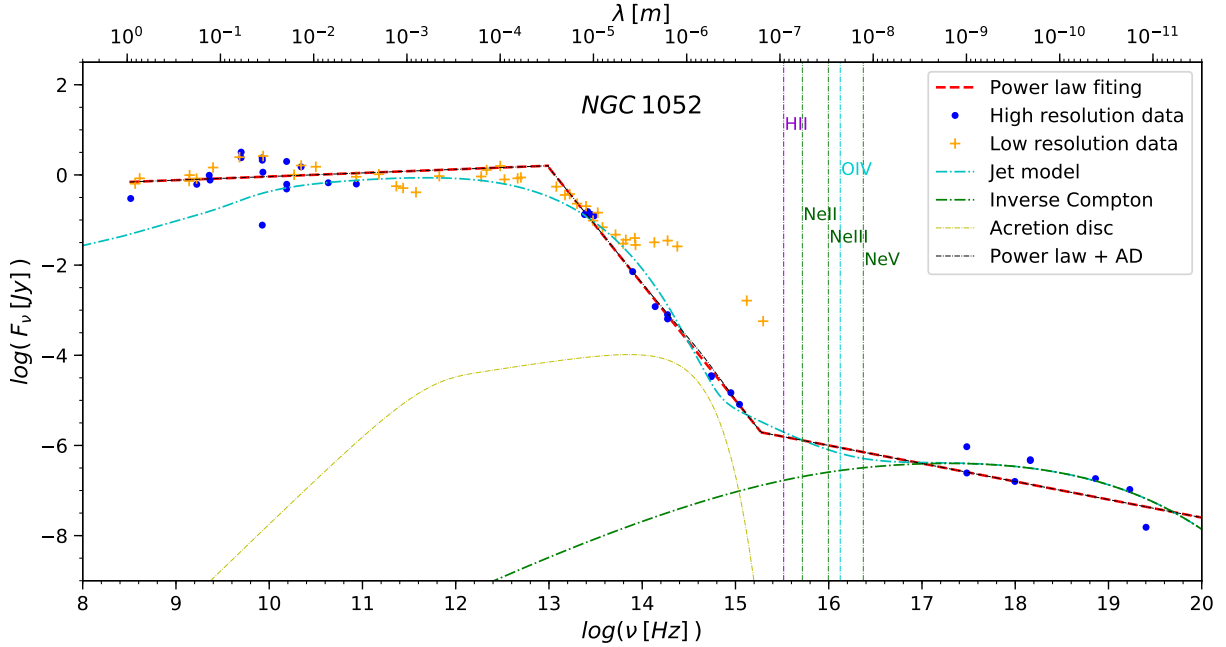


**Figure 22:** Jet model for NGC 1052. The blue line represents the total spectral emission from the jet, and the green line shows the contribution of the inverse Compton, which can be seen to dominate the jet emission in the X-ray range. The power-law plus accretion disc fit from Section 3.2 is also shown for comparison. See caption of Figure 10 for other details.

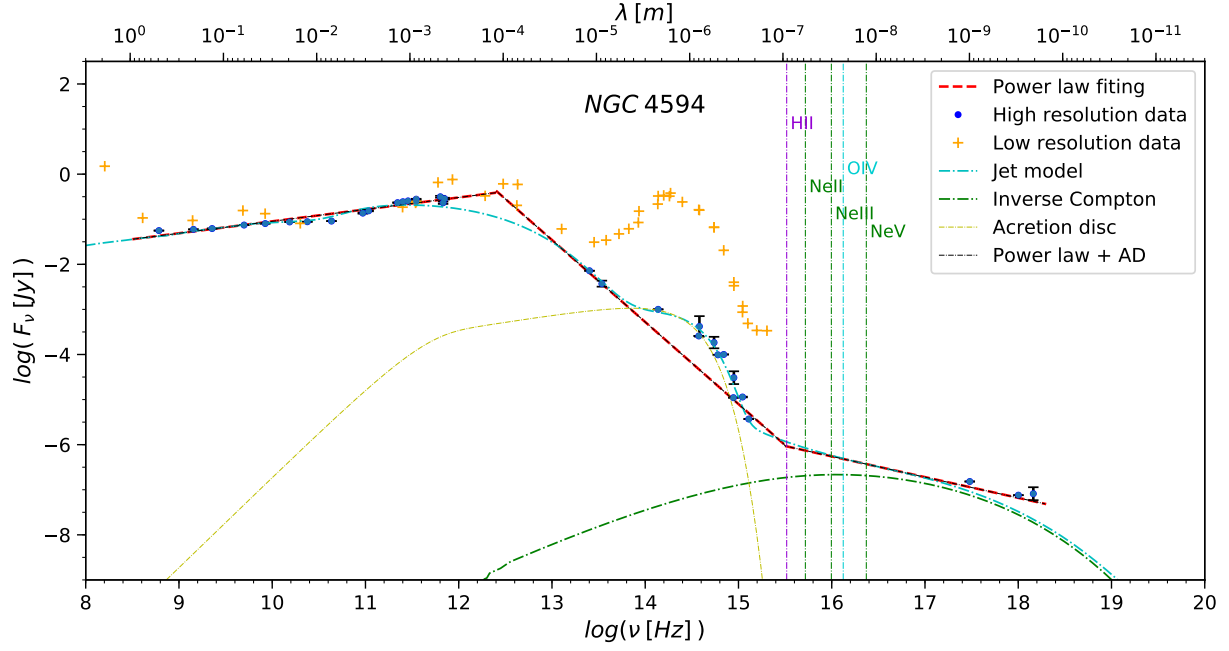


**Figure 23:** Jet model for NGC 4594. See caption of Figure 22.

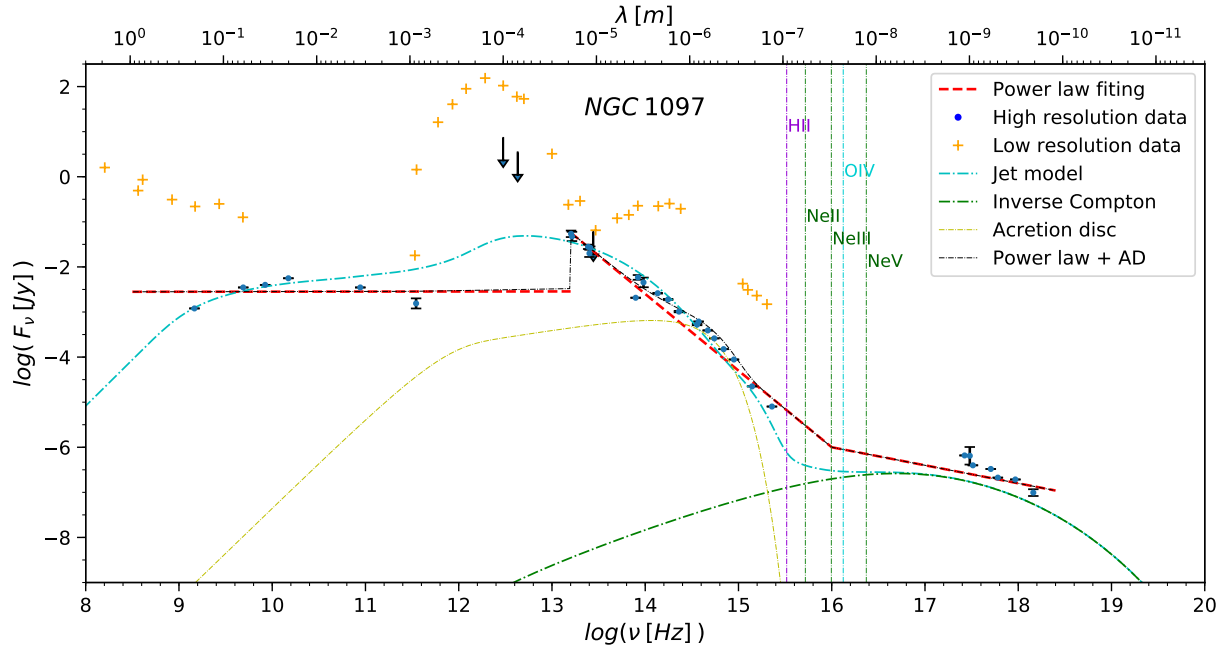


**Figure 24:** Jet model for NGC 1097. See caption of Figure 22.



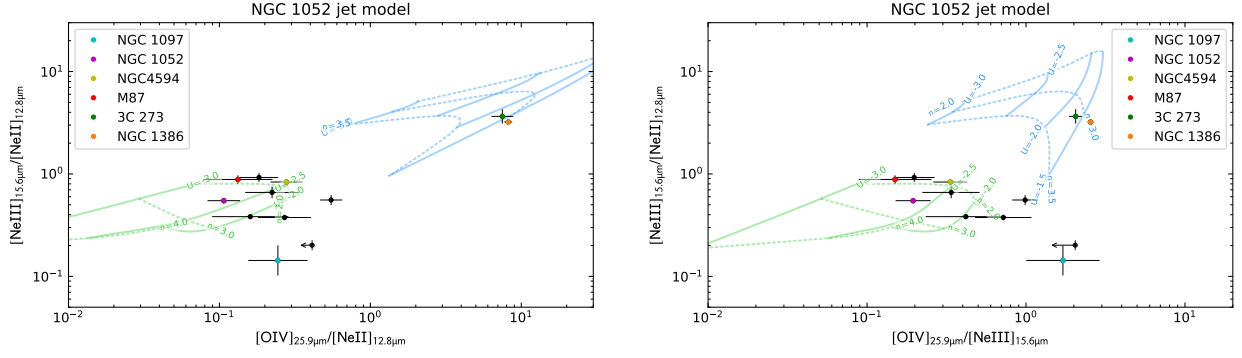


**Figure 25:** Diagnostics diagrams for the LLAGN sample overlaying the photoionisation models for NGC 1052 based on the compact jet model. See caption of Figure 15 for details.

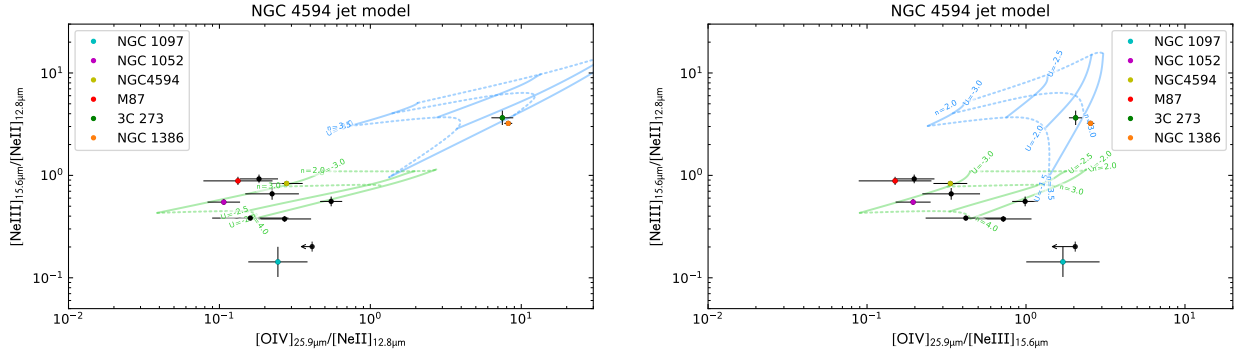


**Figure 26:** Diagnostics diagrams for the LLAGN sample overlaying the photoionisation models for NGC 4594 based on the compact jet model. See caption of Figure 15 for details.

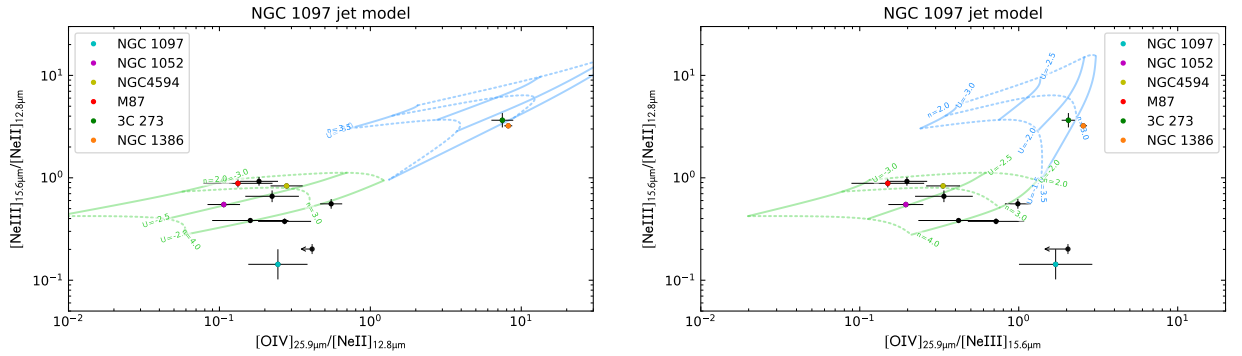


**Figure 27:** Diagnostics diagrams for the LLAGN sample overlaying the photoionisation models for NGC 1097 based on the compact jet model. See caption of Figure 15 for details.

### 3.5. Contribution of the accretion disc to the ionisation

In order to show the contribution of the accretion disc to the predicted line ratios we repeated the analysis made in Section 3.2 but excluding the accretion disc component. That is, now the input radiation field for CLOUDY is only the power law fit (red dashed line in Figure 11). We present here only the result for NGC 4594, as this is the only LLAGN in our sample where a thermal-like bump is clearly present in the SED, and therefore is the only case where a the disc contribution may be relevant to the ionisation. Figure 28 shows two diagnostics diagrams for this model, and the same diagrams for the model which includes an accretion disc (already shown in Figure 16) for an easy comparison.

It can be seen that both models produce almost identical results. This result could be anticipated, as the simulated disc for NGC 4594 is far too cold as for contributing to the ionising continuum (Figure 11). However, the contribution from this disc to the photoionisation models could not completely dismissed beforehand, because a cold disc could affect the thermal structure of the simulated cloud, and therefore indirectly influence on the line ratios.

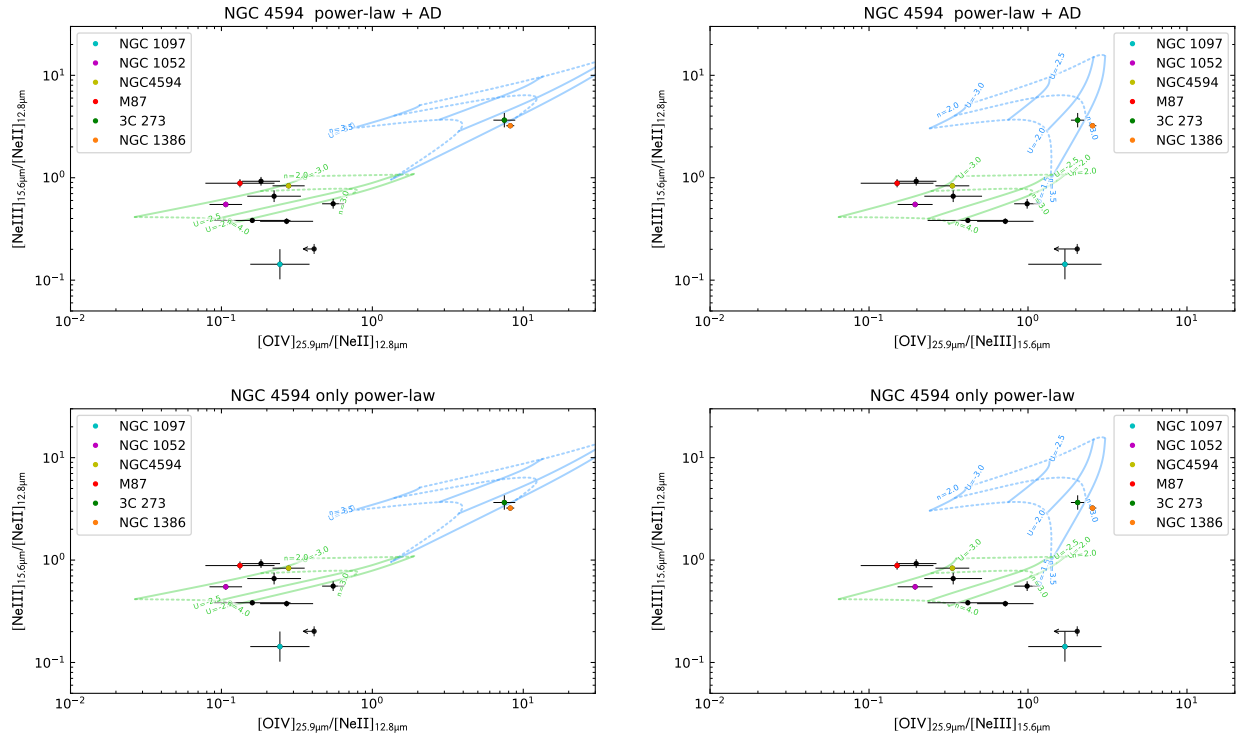


**Figure 28:** Diagnostics diagrams for the LLAGN sample overlaying photoionisation models for NGC 4594. The two above figures correspond to the model which includes an accretion disc, while the two below to the one without that disc. See caption of Figure 15 for details-

## 4. Discussion

In this section we will review the most important results exposed in Section 3, and give possible interpretations to them. The power-law models and its implication on the overall ionisation continuum of LLAGN are discussed in Section 4.1. In Section 4.2 we consider the possibility that this continuum is dominated by the emission of a compact jet. The exact contribution of the accretion disc to the ionising continuum is examined in Section 4.2. Finally, the exceptions that do not agree with the models are described in Section 4.4.

### 4.1. The Ionisation Continuum in LLAGN

In Section 3.2 the simulated emission-line ratios are able to reproduce the observed values for the nuclei in our sample of LLAGN when the continuum spectral flux is fitted as a broken power law ( $F_\nu \sim \nu^{-\alpha}$ ) plus a truncated accretion disc. This consistency between observations and simulations occurs in two ways. On the one hand, the fitted continuum of a given LLAGN is able to reproduce not only its line ratios, but also those of some of the other LLAGN, when the simulations are run with different initial conditions ( $U$  and  $n_e$ ). On the other hand, when repeating the same analysis using the fitted continuum of another LLAGN, this same behaviour is reproduced. There are notable exceptions (e.g. NGC 1097) which shall be discussed later in more detail.

In some sources, like NGC 3169, extinction makes it impossible to observe this nucleus in the visible and UV ranges. However, because of its position at the diagnostics diagrams, we can infer that the continuum emission of this object, and especially in the ionising range, must be similar to that of the 4 modelled LLAGN. The same applies to the other LLAGN.

A wide variety of excitation mechanisms has been proposed for explaining the observed line ratios of LLAGN and LINERs, like star-formation (Terlevich et al. 1992), shocks (Ho et al. 1993; Sugai & Malkan 2000) or more complex models involving turbulent accretion flows and jets (Dopita et al. 2015). Our results, supported by the high-angular resolution SED, show that the ionising continuum is consistent with a power-law interpolation from the UV to X-rays. This configuration is enough to reproduce the observed line ratios, without the need to include an additional excitation source. This is in line with the results obtained by Gabel et al. (2000) from the analysis of the optical spectrum in NGC 1052. In contrast, Dopita et al. (2015) explains the emission-line properties of the optical lines using a “double-shock” model with two different shock fronts at different densities ( $\sim 10^4$  and  $\sim 10^6 \text{ cm}^{-3}$ ). Including additional low-excitation and/or shock excited transitions such as [Fe II]25.99  $\mu\text{m}$  in our analysis could require a more complex model. However, to explain the properties of the high-excitation lines, less affected by contamination from the stellar component, only requires a single gas component and a power-law photo-ionisation continuum.

Looking at these models we can also conclude that the ionising continuum comes from a region with  $n_e \sim 10^{3-5} \text{ cm}^{-3}$ , which is coherent with observations (e.g. Netzer 2013).

As mentioned earlier, all the power-law fits from section 3.2 count with a certain degeneracy. This applies most notably to the region  $\log(\nu) \gtrsim 15$ , where both the lack of observational data and the dispersion in the X-ray flux contribute to this degeneracy. That spectral range happens to be precisely the most relevant for the CLOUDY simulations, because it determines the shape of the ionising radiation. In section 3.3 we studied how relevant this degeneracy is, by running three CLOUDY models with different spectral index in the X-ray power law,  $\alpha = 0.35, 0.45$  and  $0.55$ . Figure 21 shows the result of these simulations. It can be seen that this variation in the slope of the power law does not alter the results drastically, and in fact, all the models are

compatible with the observations. It is also worth mentioning that the predicted line ratios converge towards the quasar domain of excitation as the power law slope increases. This behaviour could be expected, as a steeper power law resembles more the typical 'blue bump' found in quasars.

## 4.2. Ionisation by a Jet Continuum

Overall, the fitted power laws are relatively flat in the radio ( $\alpha \sim 0$ ) over several orders of magnitude in frequency, and much steeper from the IR to the UV ( $\alpha \sim 2$ ). The X-ray data suggest that there is another turnover somewhere between the UV and the X-rays, and the continuum becomes flatter again ( $\alpha \sim 0.40$ ). From our studied LLAGN sample, the most representative case of this behaviour is NGC 1052, for which the steepness of the power law in the visible region was already predicted by [Rieke et al. \(1982\)](#). This characteristic flat-to-inverted shape is very similar to that produced by self-absorbed synchrotron emission, i.e. the signature of strong non-thermal radiation produced by a compact jet ([Blandford & Königl 1979](#)).

This idea is further supported by the results shown in Section 3.4. Here, instead of a simple power law, the continuum of 3 representative LLAGN was fitted using a more sophisticated model which simulates the emission from a compact jet plus a truncated accretion disc. This model was applied to NGC 1052 ([Reb et al. 2018](#)), NGC 4594 and NGC 1097 (L. Reb, priv. communication). Figures 25, 27 and 26 show that the results of these models are compatible not only with the observations, but also with the previous power-law models. This agreement was expected, as it can be seen (e.g. Figure 23) that both the jet model and the power-law fits produce very similar SEDs.

In these jet models, the predominant component shortwards of  $\lambda \sim 1000 \text{ \AA}$  is the one associated to inverse Compton<sup>8</sup> (see Figure 1 in [Reb et al. 2018](#)), which suggests that this would be the main source of ionisation in LLAGN. Under this scenario, the origin of the X-ray flux would be the inverse Compton scattering of less energetic photons by relativistic electrons accelerated by the jet. This process occurs at the BH corona, and the seed photons come from the synchrotron radiation of the jet.

We stated that in general, the sampled LLAGN exhibit a spectral index of  $\alpha \sim 0.40$  in the X-ray range. One notable exception to this is M87, for which our power-law fit gives  $\alpha \sim 1.20$ . One explanation for this is that the accelerated jet component is much stronger in this nucleus than in other LLAGN ([Prieto et al. 2016](#)).

## 4.3. The Accretion Disc Contribution

From our studied sample, NGC 4594 is the only LLAGN clearly exhibiting a thermal component which could be attributed to an accretion disc. Constraints imposed by the SED of this object force this disc to be truncated and with very low accretion rates. Hence, this is a cold disc peaking at  $\sim 1 \text{ \mu m}$ , and its contribution to ionisation should be negligible. This is tested in Section 3.5. Figure 28 shows the compared results when this disc is included or not on the input SED for CLOUDY. We can see that both models produce almost identical results. This suggests that in LLAGN the accretion disc, if existing, is too cold to be probed by an analysis based on photo-ionisation as the one carried out here. Nevertheless, the high-angular resolution SEDs impose constraints on the truncation radius and maximum accretion rate of these discs, as mentioned before. We found that these objects must have accretion discs truncated at  $r_{\text{in}} \sim 10\text{--}50 r_g$  and with a low accretion rate of  $\dot{m} \sim 10^{-5}\text{--}10^{-3} \dot{m}_{\text{edd}}$ .

<sup>8</sup>This process is called *inverse* because, as opposed to the standard Compton effect, the energy is transferred from the electrons to the photons.

It is important to note that for the very low luminosities ( $L_{\text{bol}} \lesssim 10^{42} \text{ erg s}^{-1}$ ) typical of LLAGN, accretion is not predicted to happen through such a disc (see Section 1.3.1). Although the exact mechanisms controlling accretion under these circumstances are still not well understood, the accretion flow is predicted to become radiatively inefficient, and the disc is predicted to be replaced by a RIAF below a certain truncation radius.

#### 4.4. Outliers

There are three LLAGN from our sample whose observed emission-line ratios could not be successfully reproduced by the above described photoionisation models. In this section, we offer possible explanations for this circumstance.

One of them is NGC 1386, the only nucleus in our sample of LLAGN that has not been classified as a LINER. In all diagnostics diagrams shown in Section 3, this LLAGN lies near 3C 273 and outside the photoionisation models made for the LINERs. The work of [Rodríguez-Ardila et al. \(2017\)](#) shows that this LLAGN has very powerful jets, comparable to those of highly-luminous AGN. SINFONI data reveal a very strong interaction between the jet and the ISM of its host galaxy, producing shocks which account for the ionisation and excitation of the coronal gas from the nucleus. The highest degree of ionisation in the gas is found at a distance of  $\sim 300 \text{ pc}$  from the nucleus and moving at high speeds  $> 230 \text{ km s}^{-1}$ , and cannot be explained by nuclear photoionisation ([Rodríguez-Ardila et al. 2017](#)).

Another object deserving special attention is NGC 404. For this LINER, [O IV] emission is not detected, and we only have an upper limit for the flux of this line. Furthermore, the ratio [Ne III]/[Ne II] seems exceptionally low when compared with the other LINERs (except for NGC 1097). All this is indicative of a spectrum dominated by stellar rather than nuclear activity. We arrive at the same conclusion when analysing the high-angular SED of these objects, as this is dominated by the stellar population from the IR to the UV. The singular shape of the high-resolution continuum of this object when compared to the other LLAGN could be due to the fact that its central BH is far less massive in this object ( $\sim 3 \times 10^5 M_{\odot}$ ).

Finally, the observations of NGC 1097 are not well reproduced by the models either. In this case, the most plausible explanation is contamination by the star-forming ring observed close to the nucleus, as already discussed in Section 2.3. This ring could be contributing especially to the [Ne III] line emission, which is coherent with the low [Ne III]/[Ne II] ratio observed in this LLAGN.

## 5. Conclusions

The main aim of this work is to determine the nature of the ionising continuum in LLAGN and study the possible contribution of an accretion disc in these nuclei. For this purpose, we have analysed a sample of 10 LLAGN, 9 of them being also LINERs. We selected 4 of them as representative from the whole sample, and fitted their high-resolution SEDs using a combination of power-laws and truncated accretion discs. These fits were in turn employed for constructing photoionisation models, whose output spectra could be compared with high-resolution emission-line flux observations from Spitzer/IRS. Using this approach, we arrive at the following conclusions:

- The observed ionisation could be successfully modelled by a power-law interpolation of the high-angular resolution spectral flux data plus a truncated disc component. The contribution of the disc to the ionising continuum is in all cases negligible. This was shown for NGC 4594, the only LLAGN from our sample with a clear thermal component on its SED. Additional ionisation sources, like star-formation or shocks, are not needed to explain the observed emission-line ratios.
- The photoionisation models developed for a given LLAGN reproduce the observed line ratios of other LLAGN as well. This indicates that the SEDs of these objects, and especially the ionising continuum, must have a similar shape. Therefore, the same physical processes must be responsible for ionisation in all these sources.
- The line ratios are also reproduced when the emission from a jet is assumed as the ionising continuum for the CLOUDY models. This strongly suggests that the continuum of these LLAGN is dominated by self-absorbed synchrotron emission plus Inverse Compton radiation from the BH corona. Therefore, the power-law interpolation can be interpreted as a first-order approximation of the more complex jet model, which is supported by the consistency of the results of the photoionisation models in both cases.
- If these LLAGN are powered by a classical Shakura-Sunyaev accretion disc with a mass-to-light conversion efficiency of  $\eta \approx 0.06$ , we find that this disc must be truncated at  $r_{\text{in}} \gtrsim 10\text{--}50r_g$  and powered by very low accretion rates of  $\dot{m} \lesssim 10^{-3}\text{--}10^{-5} \dot{m}_{\text{edd}}$ . However, a more likely scenario is that the thin disc is replaced in these nuclei by a radiatively inefficient accretion flow (RIAF), characterised by a lower  $\eta$ .

To sum up, we see that the emitted spectra of LLAGN is dominated by a compact jet over more than 10 orders of magnitude in frequency, whose predicted ionisation is compatible with observations. Yet, many open questions remain regarding the exact configuration of the accretion flow in these sources. Future works incorporating more complex models are needed to answer these questions. One possibility would be to replace the truncated high-efficiency disc by a less efficient disc with a RIAF on its inner radii. Shocks should be also taken into account if objects like NGC 1386 are to be properly described. For this purpose, new diagnostics diagrams using lines which are more sensitive to shocks (e.g. [Fe II]25.99  $\mu\text{m}$ ) might be employed. Finally, great advances in this field are expected with the *James Webb Space Telescope*, as it will allow us to probe these mid-IR lines in more nearby galaxies, but most importantly, it might detect higher-ionisation states in LLAGN (like [Ne V] lines, for which currently we only have upper limits) which will allow us to probe the continuum emission at higher energies ( $\sim 97$  eV) in comparison to the current limitation by [O IV] (54.9 eV).

## References

- Antonucci R., 1993, *ARA&A*, 31, 473
- Baldwin J. A., Phillips M. M., Terlevich R., 1981, *PASP*, 93, 5
- Ballantyne D. R., 2007, *Modern Physics Letters A*, 22, 2397
- Bernard-Salas J., et al., 2009, *ApJS*, 184, 230
- Blakeslee J. P., et al., 2009, *ApJ*, 694, 556
- Blandford R. D., Königl A., 1979, *ApJ*, 232, 34
- Cardelli J. A., Clayton G. C., Mathis J. S., 1989, *ApJ*, 345, 245
- Dalcanton J. J., et al., 2009, *ApJS*, 183, 67
- Dopita M. A., et al., 2015, *ApJ*, 801, 42
- Elitzur M., Ho L. C., 2009, *ApJ*, 701, L91
- Elitzur M., Shlosman I., 2006, *ApJ*, 648, L101
- Falcke H., Markoff S., 2000, *A&A*, 362, 113
- Falcke H., K rding E., Markoff S., 2004, *A&A*, 414, 895
- Ferland G. J., et al., 2017, *Rev. Mexicana Astron. Astrofis.*, 53, 385
- Fern ndez-Ontiveros, Juan Antonio Almudena Prieto, M. Acosta-Pulido, Jose Antonio Markoff, Sera Gonz lez-Mart n, Omaira 2013, *EPJ Web of Conferences*, 61, 04005
- Ferrarese L., Merritt D., 2000, *ApJ*, 539, L9
- Frank J., King A., Raine D., 2002, *Accretion Power in Astrophysics*, 3 edn. Cambridge University Press, doi:10.1017/CBO9781139164245
- Gabel J. R., Bruhweiler F. C., Crenshaw D. M., Kraemer S. B., Miskey C. L., 2000, *ApJ*, 532, 883
- Gebhardt K., Thomas J., 2009, *ApJ*, 700, 1690
- Groves B. A., Heckman T. M., Kauffmann G., 2006, *MNRAS*, 371, 1559
- Harrison C. M., 2017, Impact of supermassive black hole growth on star formation ([arXiv:1703.06889](https://arxiv.org/abs/1703.06889))
- Heckman T. M., 1980, *A&A*, 500, 187
- Heckman T. M., Best P. N., 2014, *ARA&A*, 52, 589
- Ho L. C., 1999, *ApJ*, 516, 672
- Ho L. C., 2008, *ARA&A*, 46, 475
- Ho L. C., Filippenko A. V., Sargent W. L. W., 1993, *ApJ*, 417, 63
- Ho L. C., Filippenko A. V., Sargent W. L. W., 1996, *ApJ*, 462, 183

- Jensen J. B., Tonry J. L., Barris B. J., Thompson R. I., Liu M. C., Rieke M. J., Ajhar E. A., Blakeslee J. P., 2003, *ApJ*, 583, 712
- Jovanović P., Popović L., Chartas G., 2009, *Black Holes and Galaxy Formation*, pp 249–294
- Khachikian E. E., Weedman D. W., 1971, *Astrofizika*, 7, 389
- Kormendy J., Ho L. C., 2013, *ARA&A*, 51, 511
- Kormendy J., et al., 1996, *The Astrophysical Journal*, 473, L91
- Lebouteiller V., Barry D. J., Goes C., Sloan G. C., Spoon H. W. W., Weedman D. W., Bernard-Salas J., Houck J. R., 2015, *ApJS*, 218, 21
- Lynden-Bell D., 1969, *Nature*, 223, 690
- Madau P., Dickinson M., 2014, *ARA&A*, 52, 415
- Magorrian J., et al., 1998, *AJ*, 115, 2285
- Mandel K. S., Wood-Vasey W. M., Friedman A. S., Kirshner R. P., 2009, *ApJ*, 704, 629
- Maoz D., 2007, *MNRAS*, 377, 1696
- Marconi A., Risaliti G., Gilli R., Hunt L. K., Maiolino R., Salvati M., 2004, *MNRAS*, 351, 169
- Markoff S., Nowak M. A., Wilms J., 2005, *ApJ*, 635, 1203
- Markoff S., et al., 2008, *ApJ*, 681, 905
- Martín-Navarro I., Brodie J. P., Romanowsky A. J., Ruiz-Lara T., van de Ven G., 2018, *Nature*, 553, 307–309
- Mathews W. G., Ferland G. J., 1987, *ApJ*, 323, 456
- Merloni A., Heinz S., di Matteo T., 2003, *MNRAS*, 345, 1057
- Netzer H., 2013, *The Physics and Evolution of Active Galactic Nuclei*. Cambridge University Press, doi:10.1017/CBO9781139109291
- Nicastro F., Martocchia A., Matt G., 2003, *ApJ*, 589, L13
- Padovani P., et al., 2017, *The Astronomy and Astrophysics Review*, 25
- Prieto M. A., Reunanen J., Tristram K. R. W., Neumayer N., Fernandez-Ontiveros J. A., Orienti M., Meisenheimer K., 2010, *Monthly Notices of the Royal Astronomical Society*, 402, 724
- Prieto M. A., Fernández-Ontiveros J. A., Markoff S., Espada D., González-Martín O., 2016, *MNRAS*, 457, 3801
- Prieto M. A., Fernandez-Ontiveros J. A., Bruzual G., Burkert A., Schartmann M., Charlot S., 2019, *Monthly Notices of the Royal Astronomical Society*, 485, 3264–3276
- Quataert E., 2003, *Astronomische Nachrichten*, 324, 435–443
- Reb L., Fernández-Ontiveros J. A., Prieto M. A., Dolag K., 2018, *MNRAS*, 478, L122
- Rees M. J., 1984, *ARA&A*, 22, 471
- Rees M., Phinney E., Begelman M., Blandford R., 1982, *Nature*, 295, 17



- Reunanen J., Prieto M. A., Siebenmorgen R., 2010, *Monthly Notices of the Royal Astronomical Society*, 402, 879
- Rieke G. H., Lebofsky M. J., Kemp J. C., 1982, *ApJ*, 252, L53
- Rodríguez-Ardila A., Prieto M. A., Mazzalay X., Fernández-Ontiveros J. A., Luque R., Müller-Sánchez F., 2017, *MNRAS*, 470, 2845
- Salpeter E. E., 1964, *ApJ*, 140, 796
- Schlafly E. F., Finkbeiner D. P., 2011, *ApJ*, 737, 103
- Schmidt M., 1963, *Nature*, 197, 1040
- Seyfert C. K., 1943, *ApJ*, 97, 28
- Shakura N. I., Sunyaev R. A., 1973, *A&A*, 500, 33
- Sugai H., Malkan M. A., 2000, *ApJ*, 529, 219
- Terlevich R., Tenorio-Tagle G., Franco J., Melnick J., 1992, *MNRAS*, 255, 713
- Tully R. B., Rizzi L., Shaya E. J., Courtois H. M., Makarov D. I., Jacobs B. A., 2009, *AJ*, 138, 323
- Tully R. B., et al., 2013, *AJ*, 146, 86
- Urry C. M., Padovani P., 1995, *PASP*, 107, 803
- Woo J.-H., Urry C. M., 2002, *ApJ*, 579, 530
- Yu Z., Yuan F., Ho L. C., 2011, *ApJ*, 726, 87
- Zel'dovich Y. B., 1964, *Soviet Physics Doklady*, 9, 195
- Zu Y., Kochanek C. S., Peterson B. M., 2011, *ApJ*, 735, 80
- van de Ven G., Fathi K., 2010, *ApJ*, 723, 767